Advances in Colloid and Interface Science 301 (2022) 102613

Contents lists available at ScienceDirect

Advances in Colloid and Interface Science

journal homepage: www.elsevier.com/locate/cis

Multispherical shapes of vesicles highlight the curvature elasticity of biomembranes

Reinhard Lipowsky *

Theory and Bio-Systems, Max Planck Institute of Colloids and Interfaces, Science Park Golm, 14424 Potsdam, Germany

ARTICLE INFO

Keywords:
Synthetic biosystems
Lipid bilayers
Giant vesicles
Transbilayer asymmetry
Spontaneous curvature
Multispherical patterns
Multispherical junctions

ABSTRACT

Giant lipid vesicles form unusual multispherical or "multi-balloon" shapes consisting of several spheres that are connected by membrane necks. Such multispherical shapes have been recently observed when the two sides of the membranes were exposed to different sugar solutions. This sugar asymmetry induced a spontaneous curvature, the sign of which could be reversed by swapping the interior with the exterior solution. Here, previous studies of multispherical shapes are reviewed and extended to develop a comprehensive theory for these shapes. Each multisphere consists of large and small spheres, characterized by two radii, the large-sphere radius, R_l, and the small-sphere radius, R_s. For positive spontaneous curvature, the multisphere can be built up from variable numbers N_l and N_s of large and small spheres. In addition, multispheres consisting of $N_* = N_l + N_s$ equally sized spheres are also possible and provide examples for constant-mean-curvature surfaces. For negative spontaneous curvature, all multispheres consist of one large sphere that encloses a variable number N_s of small spheres. These general features of multispheres arise from two basic properties of curvature elasticity: the local shape equation for spherical membrane segments and the stability conditions for closed membrane necks. In addition, the $(N_l + N_s)$-multispheres can form several $(N_l + N_s)$-patterns that differ in the way, in which the spheres are mutually connected. These patterns may involve multispherical junctions consisting of individual spheres that are connected to more than two neighboring spheres. The geometry of the multispheres is governed by two polynomial equations which imply that $(N_l + N_s)$-multispheres can only be formed within a certain restricted range of vesicle volumes. Each $(N_l + N_s)$-pattern can be characterized by a certain stability regime that depends both on the stability of the closed necks and on the multispherical geometry. Interesting and challenging topics for future studies include the response of multispheres to locally applied external forces, membrane fusion between spheres to create multispherical shapes of higher-genus topology, and the enlarged morphological complexity of multispheres arising from lipid phase separation and intramembrane domains.

1. Introduction

On the molecular scale, cellular membranes are based on the assembly of lipids and proteins into molecular bilayers. The lipid bilayer structure was first proposed in the 1920s for the plasma membranes of red blood cells [1] and directly observed by electron microscopy in the 1950s for many different cellular membranes [2,3]. The electron microscopy images revealed that the bilayers have a thickness of only 4 to 5 nm. In contrast, the lateral extension of these bilayers is much larger and can exceed tens or even hundreds of micrometers. One intriguing aspect of cellular membranes is their striking polymorphism, that is, their ability to attain many different shapes. This polymorphism is intimately related to the fluidity of the membranes. That biomembranes are in a fluid state became generally accepted at the beginning of the 1970ies based on three different developments: fast lateral diffusion of lipids as observed by spin-labeled lipids and steroids [4,5]; theoretical models for the curvature elasticity of fluid membranes [6–8]; and the proposal of the fluid-mosaic model [9].

The polymorphism of biomembranes can be elucidated using biomimetic model systems such as lipid bilayers and vesicles. One particularly useful model system are giant unilamellar vesicles (GUVs), the shape of which can be observed in the optical microscope and can be computed based on the theory of membrane elasticity. [10–12] A recent example for this fruitful interplay between theory and experiment are multispherical shapes of GUVs [13], which provide the main theme of this review.

* Corresponding author.
E-mail address: lipowsky@mpikg.mpg.de.

https://doi.org/10.1016/j.cis.2022.102613
Received in revised form 29 January 2022;
Available online 4 February 2022

One key parameter of biomembrane elasticity is the preferred or spontaneous curvature [1] of the membrane which arises from the transbilayer asymmetry between the two bilayer leaflets. Transbilayer asymmetry between the two leaflets can be generated by many molecular mechanisms as briefly reviewed in the following Section 2. These mechanisms include the compositional asymmetry between the two leaflets, which is ubiquitous in cellular membranes [14,15], as well as the molecular interactions between the leaflets and the adjacent aqueous buffers. One example are lipid bilayers with one leaflet exposed to a sucrose solution and the other leaflet exposed to a glucose solution. For GUV membranes, the latter mechanism has been observed to generate many multispherical shapes, see Figs. 1 and 2 [13].

Spherical shapes are also formed by liquid droplets. Indeed, droplets attain such shapes in order to minimize their interfacial area and thus their interfacial free energy. If we bring two spherical droplets into contact, we can create a transient two-sphere shape which would, however, be unstable and either decay into smaller droplets or merge into a larger droplet that will eventually relax into the shape of a single sphere. Now, imagine that we stabilize the transient two-sphere droplet by imposing a constraint on its interfacial area. Such a constraint can be achieved by a fluid membrane that encloses the two-sphere droplet. The two droplets are then enclosed by a single membrane which connects the two droplets by a closed membrane neck, thereby forming a two-sphere vesicle, see Fig. 1a. The stability of such a vesicle depends on the spontaneous curvature of the vesicle membrane and on the vesicle geometry, as explained below in some detail.

Two-sphere vesicles as in Fig. 1a represent the simplest examples for multispherical shapes. Indeed, the theory of membrane elasticity predicts stable multispherical shapes consisting of an arbirtrary number of (punctured) spheres connected by closed membrane necks [16,17]. Many of these shapes have been observed recently for GUVs that were exposed to asymmetric sugar solutions, see Figs. 1 and 2. The shapes in Fig. 1 were obtained for positive spontaneous curvature, those in Fig. 2 for negative spontaneous curvature.

The $(N_l + N_s)$-multispheres displayed in Fig. 1 are observed when the vesicle membranes are exposed to an inner solution of sucrose and to an outer solution of glucose. Thus, the two leaflets of the bilayer membranes experience different molecular interactions which generate a positive spontaneous curvature of about 1 μm^{-1}. As illustrated in Fig. 1, such a spontaneous curvature can create a large variety of multispherical shapes connecting individual spheres with positive mean curvature.

When the two aqueous solutions are swapped, i.e., when the interior solution contains glucose and the outer solution sucrose, the spontaneous curvature becomes negative leading to different multispherical morphologies as shown in Fig. 2. All of these multispheres consist of one large sphere that encloses a variable number of small spheres. For these $(1 + N_s)$-multispheres, the large sphere has a positive mean curvature whereas the small spheres are inverted spheres and have a negative mean curvature.

From a theoretical point of view, multispheres are appealing for several reasons. First, the existence of multispherical shapes highlights the curvature elasticity of fluid membranes. Indeed, these shapes arise from two basic properties of curvature elasticity: the coexistence of two spherical membrane segments with different radii and the connection of two spheres by closed membrane necks. Second, many properties of these shapes can be expressed in terms of simple equations and thus obtained from elementary calculus. In particular, the mechanical tension experienced by the membranes of the multispherical vesicles can be calculated explicitly, thereby revealing how this tension is determined by the interplay of curvature elasticity and vesicle geometry. Third, the membrane shapes considered here are intimately related to three different branches of 'serious' mathematics: constant-mean-curvature surfaces as considered in differential geometry; Steiner minimal trees as studied in mathematical graph theory; and sphere packings as elucidated in discrete geometry. On the one hand, multispherical shapes provide a direct and unexpected connection between these distinct mathematical topics. On the other hand, multispheres formed by fluid membranes provide a new and striking application of these mathematical concepts.

Some theoretical results for multispherical shapes have been reported previously [16–19]. The first two papers [18,19] described these shapes in a rather qualitative manner while the two subsequent reviews [16,17] summarized many features of multispherical membranes with positive spontaneous curvature but largely ignored those with negative spontaneous curvature. Here, the theory of multispherical shapes will be developed in a comprehensive way for both positive and negative spontaneous curvature, using the recent experimental observations in Figs. 1 and 2 as a strong incentive.

This paper is organized as follows. In the next Section 2, we will briefly review the different molecular mechanisms that are known to generate a significant spontaneous curvature. In Section 3, we first discuss some general features of multispherical shapes, thereby introducing the basic concepts of multisphere patterns and junctions. In Section 4, two curvature-elastic properties will be emphasized which are essential for the striking polymorphism of multi-sphere shapes: (i) the possible coexistence of two spherical radii on the same vesicle; and (ii) the formation and stability of closed membrane necks. Section 5 provides some examples for different $(N_l + N_s)$-patterns and small values of N_l and N_s. Section 6 is about the multisphere geometry which is governed by two polynomial equations. One important consequence of these equations is the limited range of volumes for which a certain $(N_l + N_s)$-multisphere can be formed (irrespective of its stability). Section 7 combines the stability relations for closed membrane necks with the multisphere geometry to obtain the stability regimes of multispherical shapes. Finally, the main results of the analysis are summarized in the last Section 8 together with an outlook on possible future studies.

2. Transbilayer asymmetry and spontaneous curvature

One key parameter for the formation of multispherical shapes is the preferred or spontaneous curvature which provides a quantitative measure for the transbilayer asymmetry of the membranes. Such an asymmetry can be generated by a variety of molecular and colloidal mechanisms which will be briefly reviewed in the following.

2.1. Leaflets with different densities and compositions

The presumably simplest asymmetry between the two bilayer leaflets is obtained for one-component bilayers if the leaflets differ in their molecular densities or, equivalently, in their areas per lipid. More precisely, one has to look at tensionless bilayers and at the deviations of the leaflet densities from their reference values for tensionless leaflets. Because the two leaflet tensions add up to the bilayer tension, a tensionless bilayer involves one stretched and one compressed leaflet, including the special reference state in which both leaflet tensions vanish. The corresponding stress asymmetry has been studied by molecular dynamics simulations both for planar lipid bilayers [20] and for lipid nanovesicles [21]. The simulations show that the bilayers prefer to curve in such a way that the stretched leaflet decreases its area per lipid whereas the compressed bilayer increases this molecular area, thereby decreasing the absolute value of the mechanical tensions in both leaflets.

The two leaflets may also differ in their molecular compositions and in the corresponding mole fractions. As an example, consider a two-component bilayer containing a phospholipid such as POPC and a glycolipid such as GM1 that has a relatively large head group, as shown schematically in Fig. 3a. Intuitively, one would expect that the bilayer

[1] Here and below, 'spontaneous curvature' is an abbreviation for 'spontaneous mean curvature'.

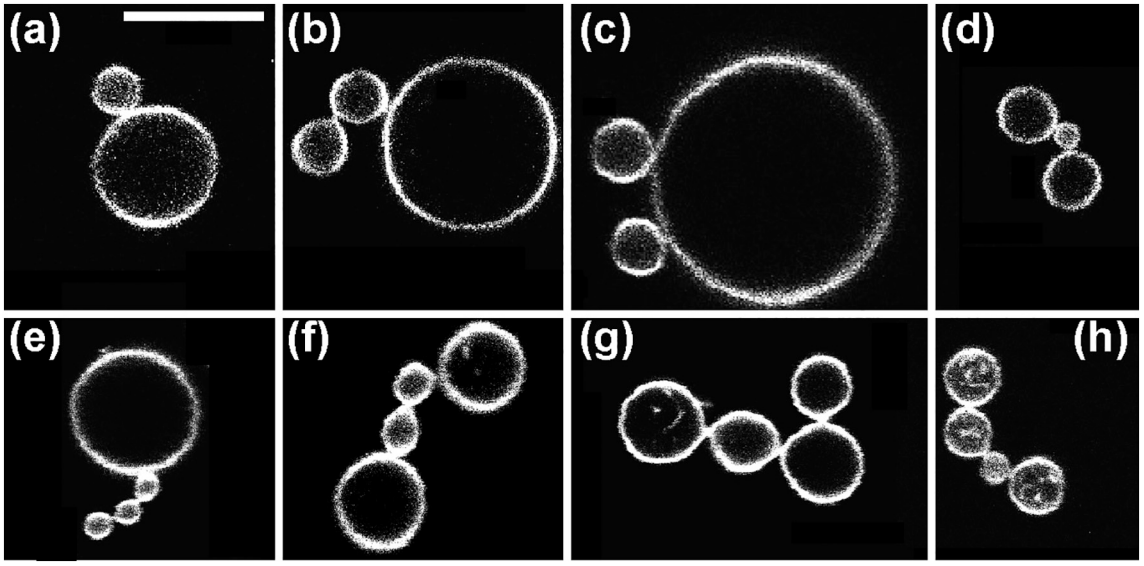

Fig. 1. Multispherical shapes of giant unilamellar vesicles (GUVs) for positive spontaneous curvature. Such multispheres are observed when the inner leaflet of the bilayer membrane is exposed to sucrose whereas the outer leaflet is in contact with glucose. Each shape involves two types of spheres, large spheres with radius R_l and small spheres with radius R_s. $(N_l + N_s)$-multispheres are obtained when the membrane forms N_l large spheres and N_s small spheres. The different panels display such multispheres with different sphere numbers N_l and N_s, apart from (b) and (c) as well as (f) and (g), which show two distinct patterns of $(1 + 2)$-spheres and of $(2 + 2)$-spheres, respectively. Scale bar in (a) is 10 μm and applies to all panels [13].

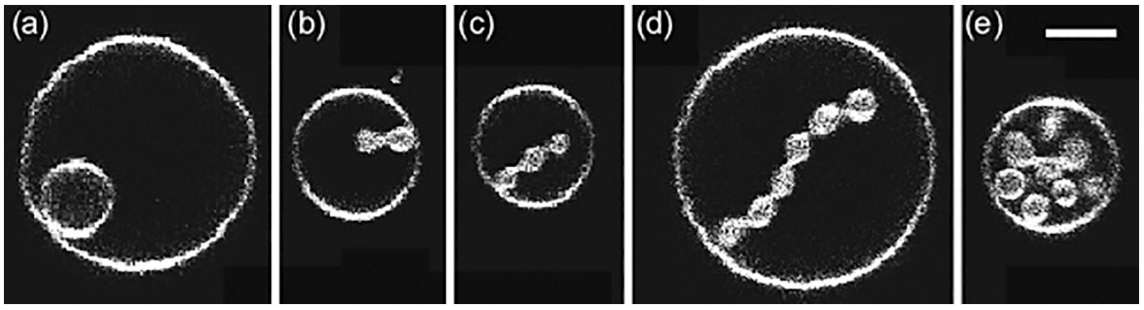

Fig. 2. Multispherical shapes of GUVs for negative spontaneous curvature. Such multispheres are observed when the inner leaflet of the bilayer membranes is exposed to glucose whereas the outer leaflet is in contact with sucrose. Each panel displays a $(1 + N_s)$-multisphere with one large sphere that encloses N_s small spheres. Scale bar in (e) is 5 μm and applies to all panels [13].

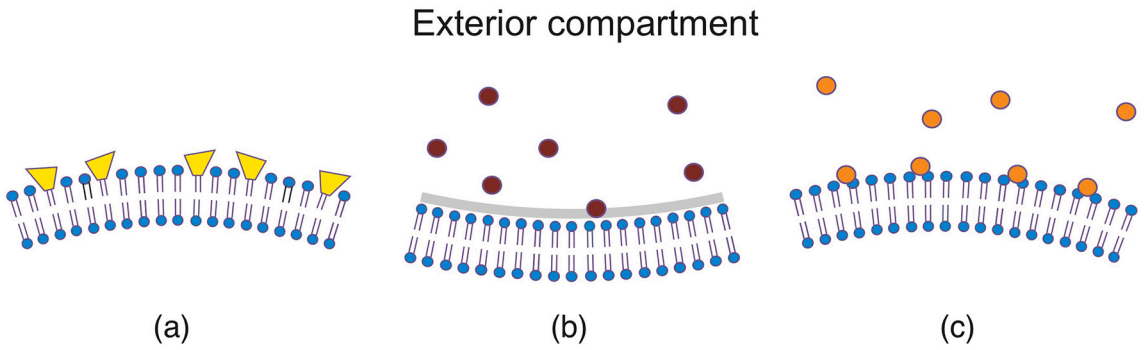

Fig. 3. Transbilayer asymmetry and spontaneous curvature arising from small molecules and solutes: (a) Compositional asymmetry between the two leaflets of the lipid bilayer with large-head group lipids (yellow) such as the glycolipid GM1 in the upper leaflet. This asymmetry leads to a positive spontaneous curvature; (b) Small solutes (purple) that do not adsorb onto the bilayer, thereby creating a depletion layer (grey) adjacent to the upper leaflet. The bilayer then prefers to bulge away from the exterior compartment which implies a negative spontaneous curvature; and (c) Small solutes (orange) that adsorb onto the upper bilayer leaflet, thereby creating an adsorption layer that induces a positive spontaneous curvature. (For interpretation of the references to color in this figure legend, the reader is referred to the web version of this article.)

prefers to bulge towards the leaflet with the higher mole fraction of the large-head-group lipid because these lipids tend to occupy more area per lipid. Even though this view does not take the constraint of vanishing bilayer tension into account, it is corroborated by molecular dynamics simulations [22–24]. In Fig. 3a, the upper leaflet has a higher mole fraction of the large-head-group lipids and is in contact with the exterior compartment which implies that the induced spontaneous curvature is positive.

2.2. Attractive and repulsive solute-membrane interactions

Somewhat different mechanisms for the generation of membrane curvature are obtained when the membrane interacts with solutes that are small compared to the bilayer thickness. The solutes may be effectively repelled from or attracted to the membrane as depicted in Fig. 3b and c, respectively. If the solutes are repelled from the membrane, they form depletion layers from which the solute molecules are excluded [25,26]. In Fig. 3b, the solutes are dissolved in the exterior compartment and then form a depletion layer in front of the upper leaflet. The depletion layer reduces the translational entropy of the small solutes. In order to decrease this entropy loss, the membrane prefers to bulge away from the exterior compartment which corresponds to a negative spontaneous curvature, see Fig. 3b.

On the other hand, if the solutes are attracted towards the membrane, they form adsorption layers in front of the bilayer leaflets, see Fig. 3c. One then expects that the membrane bulges towards the leaflet with the higher solute coverage and, thus, towards the aqueous compartment with the higher solute concentration [25,27]. The latter behavior has been observed in molecular dynamics simulations [20,28] and has been used to estimate the spontaneous curvature as generated by sucrose and glucose molecules [13], see Figs. 1 and 2.

The adsorption of divalent Ca^{2+} ions on phospholipid bilayers has led to some controversy because two experimental studies came to different conclusions about the sign of the ion-induced bilayer asymmetry. Indeed, whereas one study [29] found that the bilayer prefers to bulge towards the solution with the higher Ca^{2+} concentration, in accordance with the behavior depicted in Fig. 3c, another study [30] concluded that the Ca^{2+} adsorption layer leads to a preferred curvature in the opposite direction, i.e., that the bilayer covered with Ca^{2+} ions prefers to bulge towards the solution with the lower ion concentration. Other recent studies have provided some evidence that the area per lipid is reduced by the adsorption of Ca^{2+} ions and that this reduction becomes more pronounced for higher Ca^{2+} concentrations [31–33]. Assuming such a concentration-dependent reduction of the area per lipid, one would expect that the bilayer bulges towards the solution with the lower Ca^{2+} concentration.

2.3. Membrane scaffolding by adhesive nanoparticles

Next, consider rigid nanoparticles with a size that is large compared to the bilayer thickness. If the molecular interactions between the nanoparticle and the bilayer membrane are attractive, the particle acts as a scaffold for the shape of the membrane. The simplest example for membrane scaffolding is provided by a rigid nanoparticle with a spherical shape as depicted in Fig. 4a. In this example, the radius of the nanoparticle is about 2.5 times the thickness of the bilayer and the particle is partially engulfed by the membrane. Partial engulfment can be stabilized by a spontaneous curvature of the membrane that is opposite to the curvature of the particle-bound membrane segment [34]. In general, a nanoparticle can have many different shapes with different patterns of adhesive surface segments. Two such patterns are displayed in Fig. 4b,c. In Fig. 4b, the whole concave surface segment is adhesive (red), which leads to curvature generation after adhesion (induced fit). In Fig. 4c, the adhesive surface domains (red) are buried inside the concave part of the particle surface, and the membrane must first bend before it can bind to the particle (conformational selection).

2.4. Entropic scaffolding by anchored chain molecules

The scaffolding by rigid nanoparticles arises from the adhesion between the nanoparticles and the membrane. In contrast, the scaffolding by long chain molecules is caused by the loss of configurational entropy of the chains resulting from the steric hindrance of these chains by the membrane [35–37]. In order to stay close to the membrane, the chain molecule must, however, be anchored to the membrane. Several cases for this anchorage of a linear chain molecule need to be distinguished, see Fig. 5.

The simplest case is provided by a linear chain with a single anchor at one end as depicted in Fig. 5a. In this case, the membrane bends away from the anchored chain in order to increase the spatial region that is accessible to the other end of the chain [35,37]. On the other hand, if we anchor this other chain end to the membrane as well, see Fig. 5b, the membrane remains essentially flat because the entropic scaffolding is now limited to chain configurations, for which both anchors are close together, whereas large anchor-anchor separations stretch the chain molecule and curve the membrane in the opposite direction [36]. If the chain molecules have intermediate anchor segments as in Fig. 5c, the entropic scaffolding is limited to the loose chain ends and the membrane prefers to bend away from these ends.

2.5. Curvature generation by membrane-bound proteins

Bilayer asymmetry and spontaneous curvature can also be generated by membrane-bound proteins. A simple example is provided by His-tagged GFP proteins that bind to NTA anchor lipids. Early experimental studies addressing the curvature generation by these proteins

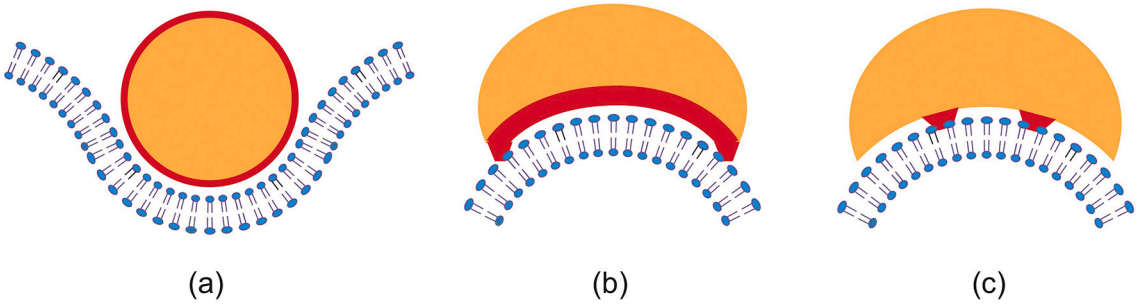

Fig. 4. Adhesion-induced scaffoding of membranes by rigid nanoparticles (orange): (a) A spherical nanoparticle with a diamater of about 10 nm and a uniform adhesive surface (red). Sufficiently strong adhesion leads to the engulfment of the particle by the membrane; and (b,c) Two types of convex-concave nanoparticles with different patterns of adhesive surface domains. (For interpretation of the references to color in this figure legend, the reader is referred to the web version of this article.)

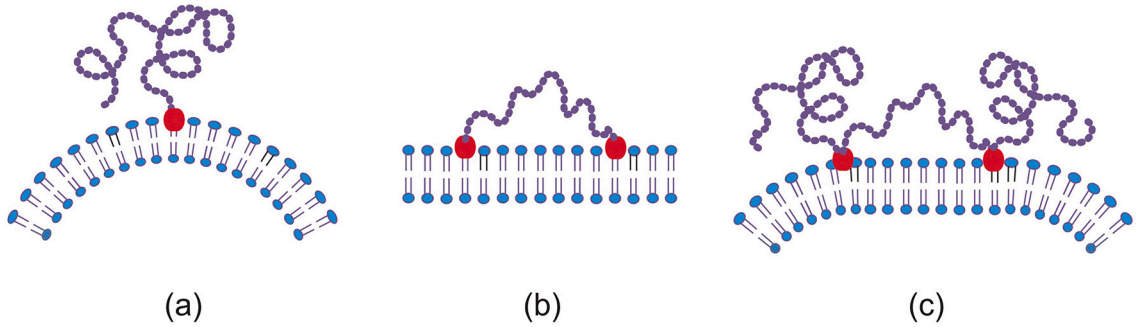

Fig. 5. Entropic scaffolding of membranes by flexible chain molecules (purple) with one or two anchor segments (red): (a) If the chain is anchored to the membrane at only one end, the membrane is bent away from the chain by the configurational entropy of the chain; (b) In contrast, the membrane remains essentially flat if the chain is anchored at both ends; and (c) For a chain with two intermediate anchor segments, the membrane is bent away from the loose chain ends as follows by combining the two cases in (a) and (b) [35,36]. (For interpretation of the references to color in this figure legend, the reader is referred to the web version of this article.)

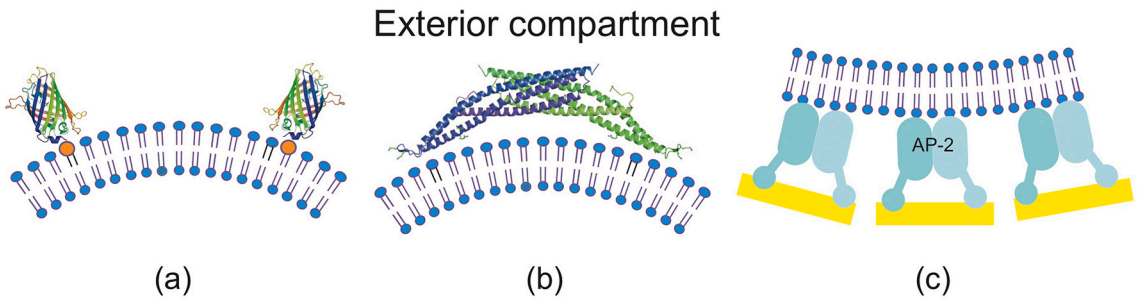

Fig. 6. Curvature generation by membrane-bound proteins: (a) Low density of His-tagged GFP bound to NTA anchor lipids (orange) in the outer bilayer leaflet [40]; (b) Homodimer of amphiphysin, providing a banana-shaped scaffold for the membrane [41–43]; and (c) Clathrin-coated pit with clathrin 'legs' (yellow) connected to the membrane via AP-2 adaptor proteins (light green) [44–47]. (For interpretation of the references to color in this figure legend, the reader is referred to the web version of this article.)

[38,39] were interpreted in terms of protein crowding. In contrast, a more recent study has demonstrated that His-tagged GFP generates a surprisingly large spontaneous curvature even in the dilute regime, in which the separation of the membrane-bound proteins is large compared to their lateral size [40], as indicated in Fig. 6a.

Another membrane-bound protein that has been shown to generate a large spontaneous curvature in the dilute regime is amphiphysin as depicted in Fig. 6b [43]. This protein forms an antiparallel homodimer [41,42] that has the shape of a banana with a curvature radius of about 11 nm and acts as a local scaffold for the adjacent membrane segment. The curvature radius of the banana-like shape suggests that, in the dense regime, the protein may generate a spontaneous curvature of up to 1/(11 nm). However, because of its anisotropic shape, the membrane-bound amphiphysin may undergo an isotropic-nematic transition at a certain critical density [27]. A third example is provided by clathrin-coated pits, see Fig. 6c, which are assembled at the membrane with the help of adaptor proteins such as AP-2 [44–47]. These coated pits represent the first step of clathrin-dependent endocytosis. The associated spontaneous curvature can be estimated from the dimensions of the clathrin-coated vesicles that are eventually formed by the endocytic process. For native coats within human cells [48], the outer diameter of the coat was found to vary between 75 and 130 nm while the enclosed vesicle had a radius between 18 and 43 nm. Thus, the spontaneous curvature of the bilayer membrane is expected to have a value between – 1/(18 nm) and – 1/(43 nm) where the negative sign reflects the endocytic process. These estimates can be used to develop a quantitative theory for the endocytosis of transferrin-coated nanoparticles [34] and to explain the non-monotonic dependence of this process on particle size as observed experimentally [49,50].

3. General features of multispheres

The previous section briefly reviewed the different molecular and colloidal mechanisms that can generate a significant spontaneous curvature of the biomembrane. Once the membrane has acquired such a curvature, it can form multispherical shapes which will now be discussed in some detail. In this introductory section, we will describe general features of the multispheres, in later sections, we will discuss their local properties, their geometry, and their stability regimes in a quantitative manner.

3.1. Each multisphere formed by a single membrane

Each multisphere as displayed in Figs. 1 and 2 is formed by a single membrane, which encloses both the spheres and the membrane necks connecting the spheres. Thus, each sphere is actually a punctured sphere and its punctures are connected to the punctures of neighboring spheres via closed membrane necks. In some cases, the time evolution of the multispherical shape has been directly observed in the microscope. One example is displayed in Fig. 7, which shows the shape transformation of a pear-like shape at time $t = 0$ to a $(1 + 1)$-multisphere with one closed membrane neck after about 15 s. If we inflated the (1+1)-multisphere osmotically, we would open up the closed neck, return to a pear-like shape, and eventually to a single large sphere.

Because each multispherical shape is formed by a single membrane, these shapes are quite different from adhesion-induced assemblies of several vesicles. Indeed, if we added a fluorescent probe to one (punctured) sphere of the multisphere, the probe would diffuse across the membrane necks and eventually spread over the whole multispherical membrane. Likewise, if we added a fluorescent probe to one of the

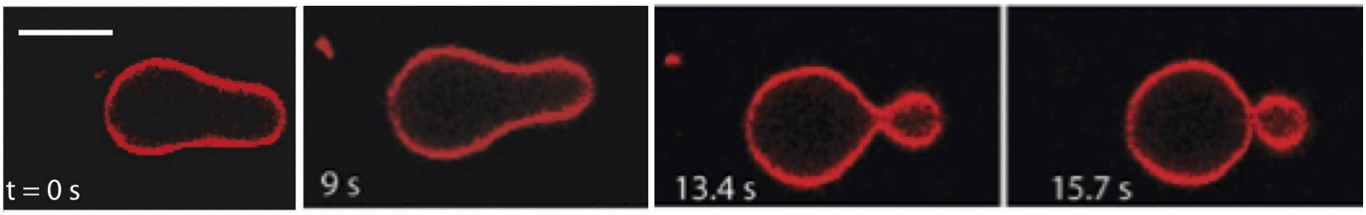

Fig. 7. Time course for the formation of a $(1 + 1)$-multisphere with one membrane neck for positive spontaneous curvature. At time $t = 0$, the GUV has a pear-like shape which develops a hour-glass waist that leads to a closed membrane neck after about 15 s. This shape transformation is observed after increasing the osmolarity in the exterior solution, thereby reducing the volume of the vesicle. Scale bar in the first image is 5 μm and applies to all images [13].

aqueous subcompartents, the latter probe would eventually spread over the whole interior compartment of the multisphere. In practise, each membrane neck will act as a bottleneck for the diffusive transport of a membrane dye from one spherical membrane segment to a neighboring one and of a water-soluble dye between aqueous subcompartments.

3.2. Multisphere patterns built up from large and small spheres

The multispheres displayed in Fig. 1 were formed for positive spontaneous curvature of the vesicle membranes. These multispheres contain large and small spheres, both of which have a positive mean curvature, as can be directly deduced from the optical images. More precisely, each multisphere involves only two types of spheres, large ones with radius R_l and small ones with radius R_s. Indeed, inspection of Fig. 1 shows that each multisphere involves only two positive values of the mean curvature as given by $M_l = 1/R_l$ for all large spheres and by $M_s = 1/R_s$ for all small spheres. Thus, each multisphere in Fig. 1 is built up from N_l large spheres and from N_s small spheres, thereby forming an $(N_l + N_s)$-multisphere. For given numbers, N_l and N_s, the small and large spheres can form distinct multisphere patterns that differ in the way, in which the spheres are mutually connected. One example for two distinct $(1 + 2)$-patterns is provided by Fig. 1b and c, another example by the two $(2 + 2)$-patterns displayed in Fig. 1f and g.

The multispheres displayed in Fig. 2 were formed for negative spontaneous curvature of the vesicle membranes. All of these patterns consist of a variable number N_s of small, inverted spheres that are enclosed by a single large sphere. These $(1 + N_s)$-multispheres can again be characterized by two radii, the radius R_l of the large sphere and the radius R_s of the small spheres but the corresponding mean curvatures have now different signs, with positive mean curvature $M_l = +1/R_l$ for

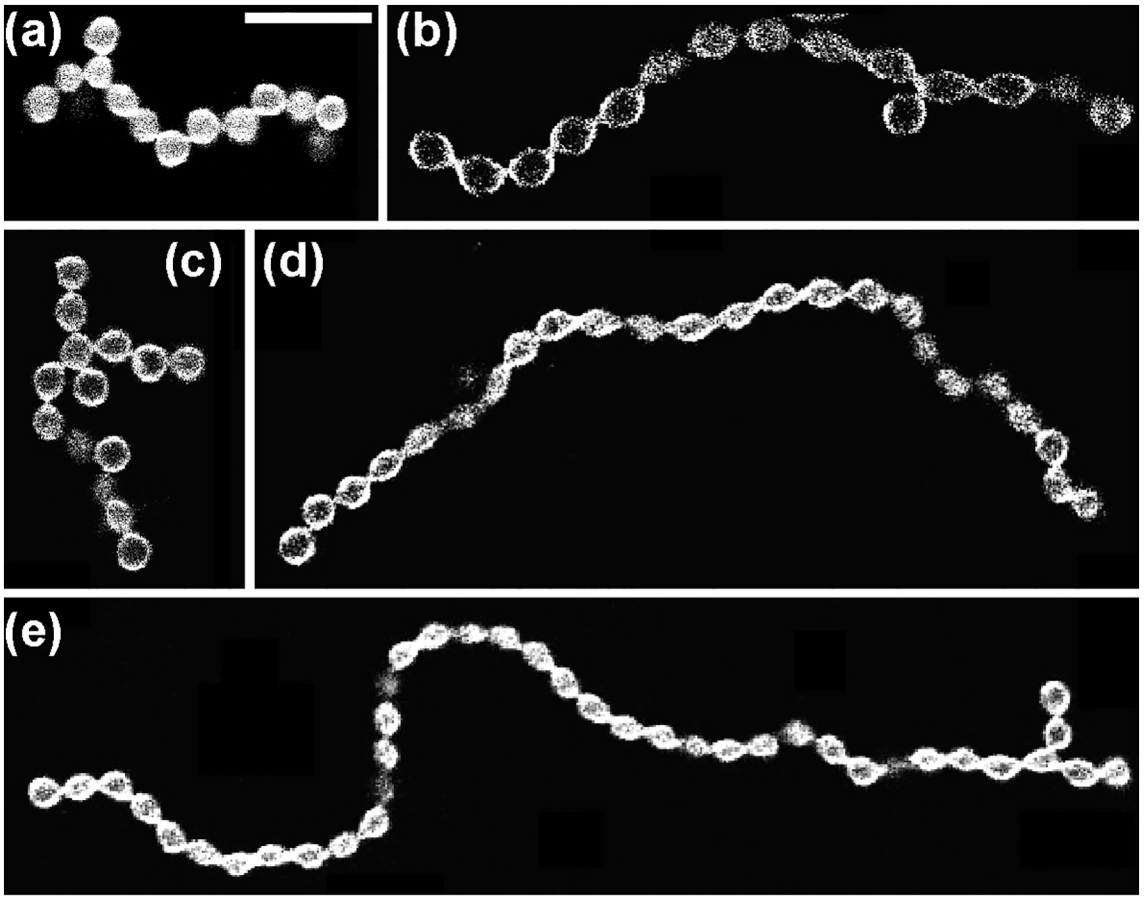

Fig. 8. Multispherical shapes consisting of N_* equally sized spheres for positive spontaneous curvature. The sphere number N_* increases from $N_* = 14$ in (a) to $N_* = 39$ in (e). All (N_*)-multispheres provide examples for constant-mean-curvature surfaces. Furthermore, apart from (d), all (N_*)-multispheres displayed here exhibit multispherical junctions. Each junction consists of one central sphere that is connected to more than two neighboring spheres. Scale bar in (a) is 10 μm and applies to all panels [13].

the large sphere and negative mean curvature $M_s = -1/R_s$ for the small, inverted spheres. For a given value of N_s, the $(1 + N_s)$-multispheres can form distinct multisphere patterns, which are again distinguished by the way in which the spheres are mutually connected.

3.3. Multisphere patterns built up from equally sized spheres

For positive spontaneous curvature, special multispheres consisting of N_* equally sized spheres are also possible. These shapes correspond to the limiting case when the large-sphere-radius R_l and the small-sphere-radius R_s become equal and the $(N_l + N_s)$-multisphere becomes an (N_*)-multisphere with $N_* = N_l + N_s$. Several examples of such multispheres are displayed in Fig. 8. Close inspection of the optical images in this figure reveals that most of these shapes involve multispherical junctions, consisting of a central sphere that is connected to more than two neighboring spheres by more than two membrane necks. For fixed sphere number N_*, several (N_*)-patterns can be distinguished that now differ in the way in which the N_* equally sized spheres are connected by the membrane necks and, thus, differ in the number of multispherical junctions and in the number of spheres between these junctions.

Each (N_*)-multisphere can be reached, in principle, via many different $(N_l + N_s)$-spheres that satisfy $N_l + N_s = N_*$. The (14_*)-multisphere displayed in Fig. 8a, for example. could be reached deflating a $(1 + 13)$-multisphere or a $(2 + 12)$-pattern or a $(3 + 11)$-pattern. Furthermore, each of these different types of multispheres can form several distinct multisphere patterns. As we will see further below, the (N_*)-multispheres have the smallest volume of all possible $(N_l + N_s)$-multispheres with $N_l + N_s = N_*$. Therefore, it should be quite interesting to study the response of an (N_*)-multisphere to an increase in its volume by osmotic inflation.

The formation of multispherical junctions is not limited to (N_*)-multispheres but has also been observed for $(N_l + N_s)$-multispheres built up from large and small spheres. Two examples for positive spontaneous curvature are displayed in Fig. 9a and b, one example for negative spontaneous curvature in Fig. 9c.

3.4. Local and global properties of multispheres

To proceed, we will now distinguish local from global properties of multispherical shapes. By definition, local properties do not depend explicitly on the numbers N_l and N_s of large and small spheres that characterize the different $(N_l + N_s)$-multispheres. Important local properties are provided by the shape equation for multispheres, by the stability conditions for closed membrane necks, and by the constriction forces acting on these closed necks, which will be discussed in the next section. In contrast, the geometry of multispheres depends explicitly on the sphere numbers N_l and N_s. This dependence is described by two polynomial relationships between these numbers, the radii R_l and R_s of large and small spheres as well as the total volume and total membrane area of the multispheres.

It is important to note that local properties may have global consequences for the membrane shapes. One example is provided by the local shape equation for multispheres to be examined in the next section. This equation determines two local properties, the total membrane tension $\Sigma_{\rm tot}$ and the pressure difference ΔP, but has the global consequence that a multisphere can involve only up two different sphere radii, irrespective of the total number of spheres. On the other hand, the effective neck mean curvature $M_{\rm ne}$, which plays an important role both for the stability of the necks and for the constriction forces acting at those necks, represents a local quantity but depends implicitly on the overall multisphere geometry as encoded in the rescaled volume v to be defined further below.

4. Shapes with two constant mean curvatures

As before, we will denote the radius of the large spheres by R_l and the radius of the small spheres by R_s. The corresponding mean curvatures of the large and small spheres are given by

$$M_l = \frac{1}{R_l} \quad \text{and} \quad M_s = \pm\frac{1}{R_s} \,. \tag{1}$$

The plus sign in the second equality applies to small spheres that have a positive mean curvature as in Fig. 1 whereas the minus sign applies to small spheres with a negative mean curvature as in Fig. 2. As shown in the next subsection, the small spheres have positive and negative mean curvatures if the membrane has positive and negative spontaneous curvatures, respectively. In contrast to the mean curvature M_s of the small spheres, the mean curvature M_l of the large spheres is always positive.

4.1. Shape equation for spherical membrane segments

The spontaneous cuvature model [7,51,52] is based on the bending energy

$$E_{\rm be} = 2\kappa \int {\rm d}A (M - m)^2 \tag{2}$$

of the membrane, which involves two membrane-elastic parameters, the bending rigidity κ and the preferred or spontaneous curvature m. In addition, the model involves two geometric parameters, the vesicle volume V and the membrane area A, as well as the associated conjugate variables provided by the pressure difference

$$\Delta P \equiv P_{\rm in} - P_{\rm ex} \tag{3}$$

between the interior and exterior compartments and the mechanical tension Σ. It is convenient to use the two variables ΔP and Σ as Lagrange multipliers in order to ensure that the vesicle shape has a certain volume and a certain area [51,52]. As a consequence, one then has to minimize the shape functional

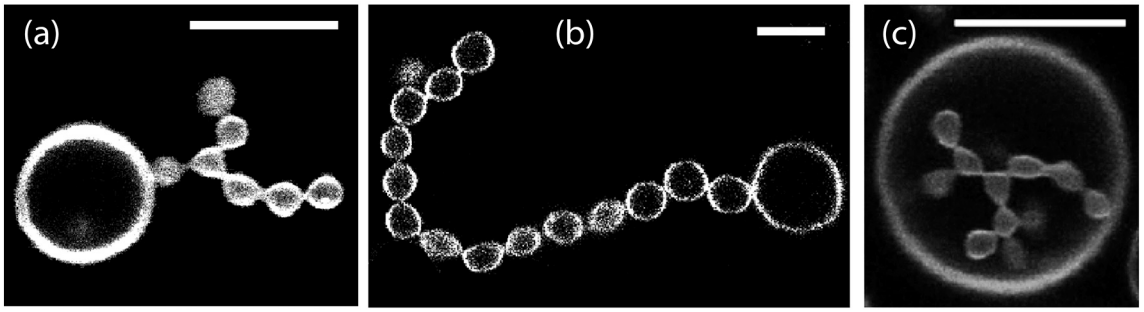

Fig. 9. $(1 + N_s)$-multispheres with junctions for (a,b) positive and (c) negative spontaneous curvature: (a) Branched chain with $N_s = 7$ small spheres forming one junction; (b) Branched chain with $N_s = 15$ small spheres and one junction, formed by the third small sphere from the upper left chain end; and (c) Branched multispherical chain with $N_s = 11$ small spheres and three junctions, enclosed by one large sphere. All scale bars: 10 μm [13].

$$F = -\Delta P\ V + \Sigma A + E_{be} \tag{4}$$

with the bending energy as given by Eq. (2).

For spherical membrane segments with mean curvature M_{sp}, the Euler-Lagrange equation of the shape functional in Eq. (4) has the form

$$\Delta P = P_{in} - P_{ex} = 2\,\Sigma_{tot}\,M_{sp} - 4\kappa m M_{sp}^2 \tag{5}$$

with the total membrane tension

$$\Sigma_{tot} = \Sigma + 2\kappa m^2\,, \tag{6}$$

which depends on the mechanical tension Σ and on the spontaneous tension [27] which is equal to $2\kappa m^2$.

The shape equation is quadratic in the mean curvature M_{sp} and can have two real-valued solutions, $M_{sp} = M_a$ and $M_{sp} = M_b$, which coexist on the same vesicle for given values of Σ_{tot} and ΔP. The two solutions of the shape Eq. (5) have the general form

$$M_a = \frac{\Sigma_{tot}}{4\kappa m} + \sqrt{\left(\frac{\Sigma_{tot}}{4\kappa m}\right)^2 - \frac{\Delta P}{4\kappa m}} \tag{7}$$

and

$$M_b = \frac{\Sigma_{tot}}{4\kappa m} - \sqrt{\left(\frac{\Sigma_{tot}}{4\kappa m}\right)^2 - \frac{\Delta P}{4\kappa m}}\,. \tag{8}$$

Furthermore, if a membrane forms spherical segments with mean curvatures M_a and M_b, a combination of the two separate shape equations for M_a and M_b leads to the total membrane tension [13,17]

$$\Sigma_{tot} = 2\kappa m(M_a + M_b) \tag{9}$$

and to the pressure difference

$$\Delta P = P_{in} - P_{ex} = 4\kappa m M_a M_b\,. \tag{10}$$

It is important to note that the total membrane tension Σ_{tot} and the pressure difference ΔP depend on the combination κm of the two membrane-elastic parameters κ and m as well as on the mean curvatures M_a and M_b of the two types of spheres. This interplay between curvature-elasticity and vesicle geometry also applies to the mechanical membrane tension $\Sigma = \Sigma_{tot} - 2\kappa m^2$ that will be examined in some detail further below.

The two solutions M_a and M_b in Eqs. (7) and (8) are real-valued as long as the discriminant under the square root is non-negative which is equivalent to the condition

$$\Sigma_{tot}^2 \geq 4\kappa m \Delta P\,. \tag{11}$$

When we express the total membrane tension Σ_{tot} and the pressure difference ΔP in terms of M_a and M_b via Eqs. (9) and (10), we find that the inequality in Eq. (11) can be rewritten in the form $(M_a - M_b)^2 \geq 0$ which is always fulfilled irrespective of the signs of M_a and M_b.

For the limiting case $\Sigma_{tot}^2 = 4\kappa m \Delta P$, the two solutions M_a and M_b in Eqs. (7) and (8) become identical and lead to the single solution $M_a = M_b = M_*$ with

$$M_* = \frac{\Sigma_{tot}}{4\kappa m} = \sqrt{\frac{\Delta P}{4\kappa m}}, \tag{12}$$

corresponding to a multisphere that is built up from a certain number of equally sized spheres with constant mean curvature M_* as in Fig. 8.

4.1.1. Multispheres for positive spontaneous curvature

For positive spontaneous curvature, $m > 0$, the membrane prefers to form shapes with positive mean curvature. In fact, all multispherical shapes displayed in Fig. 1 consist of large and small spheres, both of which have positive mean curvature. Denoting the mean curvature of the large and small spheres by M_l and M_s with $M_s > M_l$, the general solution in Eqs. (7) and (8) leads to

$$M_l = M_b \quad \text{and} \quad M_s = M_a \quad \text{for}\, m > 0. \tag{13}$$

It then follows from Eqs. (9) and (10) that the total membrane tension Σ_{tot} and the pressure difference ΔP are positive as well. Vice versa, for $\Delta P > 0$ and $\Sigma_{tot} > 0$, both solutions $M_l = M_b$ and $M_s = M_a$ as given by Eqs. (8) and (7) are positive for positive spontaneous curvature, $m > 0$. Thus, we conclude that $m > 0$ leads to multispherical shapes with positive mean curvatures of all individual spheres, which experience a positive total tension $\Sigma_{tot} > 0$ and a positive pressure differene $\Delta P > 0$.

4.1.2. Multispheres for negative spontaneous curvature

The multispherical shapes in Fig. 2 consist of one large sphere with radius R_l and a variable number of small and inverted spheres with radius R_s. In this case, the large sphere has positive mean curvature, $M_l > 0$, whereas the small and inverted spheres have negative mean curvature $M_s < 0$ which implies that

$$M_l = \frac{1}{R_l} > 0 \quad \text{and} \quad M_s = -\frac{1}{R_s} < 0\,. \tag{14}$$

Comparison with the general solution in Eqs. (7) and (8) now leads to

$$M_l = M_a \quad \text{and} \quad M_s = M_b \quad \text{for}\, m < 0. \tag{15}$$

Furthermore, for a membrane shape without self-intersections, the radius R_s of the small spheres must satisfy $R_s \leq R_l$ which implies

$$M_a + M_b = M_l + M_s = \frac{1}{R_l} - \frac{1}{R_s} \leq 0\,. \tag{16}$$

Using this inequality together with $m < 0$ in Eq. (9) for the total membrane tension Σ_{tot}, we conclude that Σ_{tot} is again positive. Likewise, it also follows from Eq. (10) for the pressure difference ΔP that this difference is positive for $m < 0$, $M_l = M_a > 0$, and $M_s = M_b < 0$.

Vice versa, if we examine the two solutions M_a and M_b in Eqs. (7) and (8) for negative spontaneous curvature $m < 0$, positive total membrane tension, $\Sigma_{tot} > 0$, and positive pressure difference, $\Delta P > 0$, we obtain $M_a > 0$ from Eq. (7) and $M_b < 0$ from Eq. (8). Thus, we conclude that a negative spontaneous curvature leads to multispherical shapes with one large sphere of positive mean curvature $M_l = M_a > 0$ and a variable number of small, inverted spheres with negative mean curvatures $M_s = M_b < 0$. In addition, both the large sphere and the small, inverted spheres experience a positive total tension $\Sigma_{tot} > 0$ and a positive pressure differene $\Delta P = P_{in} - P_{ex} > 0$.

4.2. Digression: constant-mean-curvature surfaces

As mentioned, multispheres consisting of N_* equally sized spheres, see Fig. 8, represent constant-mean-curvature (CMC) surfaces with mean curvature $M = M_*$ as in Eq. (12). Constant-mean-curvature (CMC) surfaces have been studied in differential geometry for a long time, generalizing the concept of minimal surfaces with constant mean curvature $M = 0$. The classic example for CMC surfaces are soap films and soap bubbles, the shape of which is governed by the Laplace equation

$$\Delta P = P_{in} - P_{ex} = 2\Sigma_{int} M \tag{17}$$

with the interfacial tension Σ_{int}. The Laplace equation is linear in the mean curvature M and determines the shape of interfaces exposed to the pressure difference ΔP between the interior and the exterior compartment. This equation follows from the first variation of the shape functional

$$F_{int} = -\Delta P\ V + \Sigma_{int} A\,, \tag{18}$$

which has the same form as the first two terms of the shape functional

for membranes in Eq. (4). However, the second term now represents the interfacial free energy which depends on the interfacial tension $\Sigma_{\rm int}$. The latter tension is a material parameter which must be postive as required by the thermodynamic stability of liquid- liquid interfaces. In contrast, the mechanical tension Σ in Eq. (4) depends on the geometry of the membrane and can attain both positive and negative values corresponding to stretched and compressed membranes.

For $\Delta P = 0$, the Laplace equation (17) describes a minimal surface with $M = 0$. For a long time, the only examples for freely suspended CMC surfaces with $M \neq 0$ were provided by the unduloids of Delaunay [53], which provide a one-parameter family of tubular shapes that interpolate smoothly between multispherical tubes consisting of equally sized (and punctured) spheres and cylindrical tubes. More recently, additional CMC surfaces have been constructed by pertubing a cluster of identical spheres that touch each other [54–58]. One example are triunduloids [57,58] that consist of three unduloidal arms connected by a central core.

In the research field of CMC surfaces, the physical system typically used to motivate these surfaces are the shapes of soap films and liquid droplets. However, when the initial cluster of identical and touching spheres is viewed as a cluster of liquid droplets, the resulting CMC surface is not stable. Indeed, the cluster will either fall apart and then form many small droplets or it will coalesce into one large droplet that will eventually attain the shape of a single sphere. However, when the initial cluster of droplets is enclosed by a membrane, this membrane can lead to a stable multispherical shape as considered here.

4.3. Vesicle shapes with one constant mean curvature

To reveal the general relationship between CMC surfaces with one constant mean curvature and membrane shapes, we start from the first variation of the shape functional F in Eq. (4) which leads to the Euler–Lagrange equation [59]

$$\Delta P = 2\,\Sigma\,M - 2\kappa\,\nabla^2_{\rm LB} M - 4\kappa[M-m][M(M+m) - G] \tag{19}$$

with the Laplace-Beltrami operator $\nabla^2_{\rm LB}$ and the (local) Gaussian curvature G. The Laplace-Beltrami term vanishes for constant values of the mean curvature M. In fact, for constant M, all terms in Eq. (19) become constant as well, apart from the last term proportional to the Gaussian curvature. Indeed, the Gaussian curvature G can still vary along the surface even for constant M. One example for such a spatial variation of G is provided by unduloids [60]. However, when we choose the constant mean curvature M to be equal to the spontaneous curvature m, we arrive at the simplified shape equation

$$\Delta P = 2\,\Sigma\,M = 2\Sigma m \quad \text{with}\, M = m. \tag{20}$$

Therefore, we conclude that a CMC surface with constant mean curvature $M = m$ satisfies the general Euler-Lagrange equation (19) of the spontaneous curvature model. Multispherical shapes with $M = M_* = m$ provide a special example for this general property. In the morphology diagram to be discussed further below, these CMC shapes correspond to special corner points of the stability regimes for $(N_l + N_s)$-multispheres.

A CMC surface with $M = m$ has zero bending energy $E_{\rm be}$ as follows from the form of this energy in Eq. (2). Because the bending energy density $2\kappa(M-m)^2$ cannot be negative, a membrane that forms a CMC surface with $M = m$ and $E_{\rm be} = 0$ has the lowest possible bending energy of all possible shapes.

Red blood cells sometimes form thin tube-like protrusions or myelin forms [61], which have been compared to unduloids with $M = m$ [62]. It should be noted, however, that the theoretical study in Ref. [62] did not include multispherical tubes as considered here because of the small-scale cutoff as provided by the bilayer thickness for the radius of the membrane neck. This issue will be addressed in the next section when we discuss the shape of membrane necks on the nanoscale.

Tubular membrane shapes that resemble unduloids have also been observed in the nonequilibrium context of the pearling instability [63]. The theories used to describe this instability were first based on the assumption of zero spontaneous curvature [64] and were later extended to nonzero values of the spontaneous curvature [65]. The experimentally observed tubes reported in Refs. [63] and [65] developed pearls or bulges that moved along the tubes or underwent complex relaxation processes, directly demonstrating the nonequilibrium character of these tubes. On the other hand, one tube segment displayed in Fig. 5 of Ref [63] looks like a multispherical tube consisting of alternating large and small spheres, which represents a possible (meta)stable shape as follows from the theory described here. Thus, it is conceivable that the pearling instability can be used to generate stable multispherical tubes but whether such an approach is experimentally feasible remains to be seen.

5. Local properties of membrane necks

As explained before, the spheres in Figs. 1 and 2 are punctured spheres with their punctures being connected by closed membrane necks. On the nanoscale, the outer diameter of a closed neck is about 8 to 10 nm, corresponding to the thickness of two adjacent lipid bilayers. Such a nanoscopic diameter cannot be resolved by conventional optical microscopy. Therefore, the fine structure of the necks cannot be detected in the optical images of Figs. 1 and 2.

Closed necks were first identified theoretically in the context of limit shapes as obtained from numerical solutions for axially symmetric shapes [52]. These limit shapes are characterized by shape contours that develop a point-like kink at which the curvature is ill-defined. Limit shapes with one neck have also frequently been observed in experimental studies. One example is provided in Fig. 7 which displays the time-dependent shape transformation of a pear-shaped vesicle into a two-sphere vesicle with a closed membrane neck. In this example, the neck closure process was induced by osmotic deflation, i.e., by increasing the sugar concentration and thus the osmotic pressure in the exterior solution, which leads to a reduction of the vesicle volume. In addition to limit shapes that originate from the closure of membrane necks as in Fig. 7, another type of limit shape is caused, for positive spontaneous curvature, by the limited range of volumes for which the multispherical geometry is possible.

5.1. Mean curvature of closed necks

Consider two punctured spheres with mean curvatures M_a and M_b. When these two spheres are connected by a closed neck, this neck can be characterized by the (effective) mean curvature $M_{\rm ne}$ which is defined by

$$M_{\rm ne} \equiv M_{\rm ab} \equiv \frac{1}{2}(M_a + M_b) = \frac{1}{2}\left(\frac{1}{R_a} \pm \frac{1}{R_b}\right). \tag{21}$$

This definition will be used both for necks between large and small spheres with $a = l$ and $b = s$ as well as for two identical spheres with $a = b = l$ or $a = b = s$ or $a = b =$*, where the last case applies to the necks of multispheres consisting of equally sized spheres.

Closed membrane necks look quite different when we view them with nanoscale and with micron scale resolution. These two different views are displayed in Fig. 10. In panels (a) and (b) of this figure, we see a closed membrane neck at the nanoscale, as observed in molecular dynamics simulations. The lipid bilayer has a thickness of about 4 nm and forms a neck with an hourglass-like shape. The neck is axisymmetric and has a circular waistline. For a closed neck, the outer radius of this waisline is equal to twice the bilayer thickness whereas the inner radius vanishes. For the examples shown in Fig. 10a,b the vesicle size is about 36 nm, which is the diameter of the spherical vesicle that we would obtain from the dumbbell-shaped vesicle by osmotic inflation. Inspection of the simulation snapshots shows that the hourglass-shaped neck is highly curved in the sense that its contour curvature is large and negative.

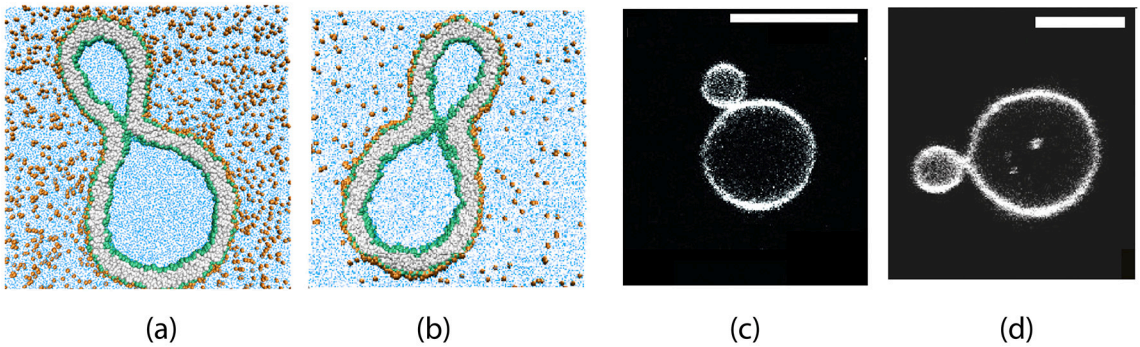

Fig. 10. Closed membrane necks viewed on nano and micron scales: (a,b) Two examples for the hourglass-like shape of closed necks on the nanoscale where we can see the molecular bilayers. Both exterior solutions contain small solutes such as simple sugars (orange) [28]: a large solute concentration for good solvent conditions in (a) and a small concentration for poor solvent conditions in (b); and (c,d) Optical images of giant two-sphere vesicles which are connected by a closed membrane neck that is not directly visible. Scale bars: 10 μm in (c) and 5 μm in (d). (For interpretation of the references to color in this figure legend, the reader is referred to the web version of this article.)

At the micron scale, the view of the membrane neck as obtained by optical microscopy is quite different, see panels (c) and (d) in Fig. 10. Indeed, when viewed with optical microsopy, the hourglass-shaped membrane segment is no longer visible but is replaced by the touching point of the two spheres connected by the neck. Thus, one might view the point-like neck as a direct consequence of the limited optical resolution. It turns out, however, that this point-like neck correctly captures two important aspects of the neck. First, during neck closure, the two principal curvatures diverge but the mean curvature attains a finite limit. Second, this mean curvature of the neck is directly related to the curvature radii of the two adjacent membrane segments which can be obtained from the optical images.

5.2. Closure of hourglass-shaped neck

We will now discuss the closure of the hour-glass shape in more detail. In Fig. 10a, the waistline (wl) of the hourglass-shaped neck forms a circle with radius $R_{\rm ne}$. Along this waistline, the neck is characterized by two principal curvatures, the negative contour curvature $C_{1,\rm wl} < 0$ perpendicular to the waistline and the positive principal curvature $C_{2,\rm wl} = 1/R_{\rm ne} > 0$ parallel to the waistline. When the neck closes, the neck radius goes to zero and the principal curvature $C_{2,\rm wl}$ diverges. However, the mean curvature

$$M_{\rm wl} = \frac{1}{2}(C_{1,\rm wl} + C_{2,\rm wl})$$

remains finite and satisfies the asymptotic equality

$$M_{\rm wl} \approx M_{\rm ne} \equiv \frac{1}{2}(M_a + M_b) \qquad (22)$$

in the limit of small $R_{\rm ne}$ [66], with the mean curvature $M_{\rm ne}$ of the closed neck being determined by the mean curvatures M_a and M_b of the two membrane segments adjacent to the neck. Thus, as the neck closes, the positive singular contribution from the second principal curvature $C_{2,\rm wl} = 1/R_{\rm ne} > 0$ is cancelled by another negative contribution arising from the contour curvature $C_{1,\rm wl}$, a cancellation that corresponds to the singular shape of a catenoid with vanishing neck radius. The remaining regular neck curvature $M_{\rm ne}$ may be positive or negative depending on the two mean curvatures, M_a and M_b, of the adjacent membrane segments. When these membrane segments are provided by two punctured spheres, the neck curvature in Eq. (22) can be expressed in terms of the sphere radii, leading back to the neck curvature of multispherical shapes as described by Eq. (21).

5.3. Curvature and stability of interior necks

Inspection of Fig. 1 for positive spontaneous curvature shows that all membrane necks are interior necks in the sense that they provide connections between two interior compartments, as schematically shown in Fig. 11a. Further inspection of Fig. 1 also reveals that a single multisphere can involve different types of necks. One example is provided by the (1 + 2)-multisphere in Fig. 1b which involves one *ls* neck between the large sphere and one of the small spheres as well as one *ss* neck between the two small spheres. The latter shape is also displayed in Fig. 11b where the two different types of necks are labeled explicitly. In addition, an *ll* neck connecting two large spheres is also possible, for an example see Fig. 1h.

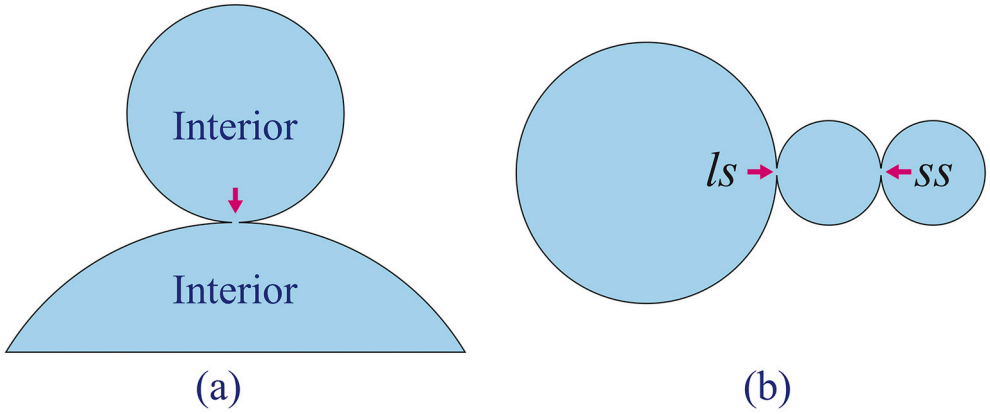

Fig. 11. Interior necks of multispherical shapes formed by membranes with positive spontaneous curvature, $m > 0$: (a) Interior membrane neck (red arrow) which connects two interior aqueous compartments (blue); and (b) A (1 + 2)-multisphere consisting of one large and two small spheres connected by two types of interior necks (two red arrows), one *ls* neck between the large and one of the small spheres, and one *ss* neck between the two small spheres. All (punctured) spheres in (a) and (b) have positive mean curvature. For $m > 0$, two large spheres can also be connected by an *ll* neck as in Fig. 1h. (For interpretation of the references to color in this figure legend, the reader is referred to the web version of this article.)

5.3.1. Mean curvature of interior necks

The three types of necks, which can be formed for positive spontaneous curvature, are governed by three different neck curvatures. An *ss* neck has the curvature

$$M_{\rm ss} \equiv \frac{1}{2}(M_s + M_s) = \frac{1}{R_s}\,, \tag{23}$$

the curvature of an *ls* neck is equal to

$$M_{\rm ls} \equiv \frac{1}{2}(M_l + M_s) = \frac{1}{2}\left(\frac{1}{R_l} + \frac{1}{R_s}\right), \tag{24}$$

and the curvature of an *ll* neck has the form

$$M_{\rm ll} \equiv \frac{1}{2}(M_l + M_l) = \frac{1}{R_l}\,. \tag{25}$$

By definition, the size of a small sphere is smaller than or equal to the size of a large sphere, that is, $R_s \le R_l$. As a consequence, the three possible curvatures of interior necks satisfy the inequalities

$$0 < M_{\rm ll} \le M_{\rm ls} \le M_{\rm ss} \quad \text{for } m > 0. \tag{26}$$

5.3.2. Stability relations for interior necks

Interior necks as in Fig. 11 are stably closed provided the spontaneous curvature m is positive and sufficiently large. More precisely, a closed interior neck with mean curvature $M_{\rm ne} = M_{ab}$ is stable if the spontaneous curvature m exceeds the neck curvature, i.e., if

$$m \ge M_{\rm ab} = \frac{1}{2}\left(\frac{1}{R_a} + \frac{1}{R_b}\right) \quad \text{(stability of interior neck)}, \tag{27}$$

as follows from Eq. (37) further below. The equality $m = M_{ab}$ describes the closure of the neck which opens up for $m < M_{ab}$. For giant vesicles, the neck curvature can be directly obtained from the microscopy images of the multispherical vesicles as in Figs. 1, 7, and 8, which provides a simple and useful approach to estimate the spontaneous curvature m experimentally [13,40].

The stability relation in Eq. (27) applies to all three types of necks with $R_a = R_l$ or $R_a = R_s$ and $R_b = R_l$ or $R_b = R_s$. The corresponding neck curvatures M_{ll}, M_{ls}, and M_{ss} satisfy the inequalities $0 < M_{ll} \le M_{ls} \le M_{ss}$. As a consequence, all necks are closed if the spontaneous curvature is sufficiently large and satisfies

$$0 < M_{\rm ll} \le M_{\rm ls} \le M_{\rm ss} \le m \quad \text{(all interior necks stably closed)} \tag{28}$$

whereas all necks are unstable against neck opening for

$$0 < m < M_{\rm ll} \le M_{\rm ls} \le M_{\rm ss} \quad \text{(all interior necks open up)}. \tag{29}$$

5.4. Curvature and stability of exterior necks

Some multispheres as observed for negative spontaneous curvature are displayed in Fig. 2. All membrane necks of these multispheres are exterior necks in the sense that they connect two exterior compartments, as schematically shown in Fig. 12a. Further inspection of Fig. 2 also reveals that a single multisphere can involve only two different types of necks. One example is provided by the (1 + 2)-sphere in Fig. 2b which involves one *ls* neck between the large sphere and one of the small, inverted spheres as well as one *ss* neck between the two small, inverted spheres. The latter shape is also displayed in Fig. 12b where the two different types of necks are labeled explicitly. In contrast to multispheres with positive spontaneous curvature, *ll* necks connecting two large spheres with positive mean curvature are *not* possible for negative spontaneous curvature.

5.4.1. Effective mean curvature of exterior necks

The two types of necks in Fig. 12b are governed by two different neck curvatures. An *ss* neck between two small, inverted spheres has the negative curvature

$$M_{\rm ss} \equiv \frac{1}{2}(M_s + M_s) = -\frac{1}{R_s} < 0\,. \tag{30}$$

Likewise, the curvature of an *ls* neck is given by

$$M_{\rm ls} \equiv \frac{1}{2}(M_l + M_s) = \frac{1}{2}\left(\frac{1}{R_l} - \frac{1}{R_s}\right) \le 0\,. \tag{31}$$

The case $M_{ls} = 0$ applies to the limiting case with $R_s = R_l$ corresponding to a small inverted sphere that has the same radius as the large sphere. Furthermore, because the radius R_s of the small spheres satisfies $R_s \le R_l$, the curvature of the *ss* and *ls* necks satisfy the inequalities

$$M_{\rm ss} \le M_{\rm ls} \le 0 \quad \text{for } m < 0. \tag{32}$$

5.4.2. Stability relations for exterior necks

Exterior necks as in Fig. 12 are stably closed if the spontaneous curvature m is negative with a sufficiently large absolute value $|m|$. Indeed, the closed neck condition now has the form

$$m \le M_{\rm ab} = \frac{1}{2}\left(\frac{1}{R_a} - \frac{1}{R_b}\right) \quad \text{(stability of exterior neck)}, \tag{33}$$

as follows from Eq. (37) further below. Because the neck curvature M_{ab} is always negative for exterior necks, the inequality in Eq. (33) can only be fulfilled if the spontaneous curvature m is negative as well. The equality $m = M_{ab}$ again describes the closure of the neck which now opens up for $M_{ab} < m$.

The stability relation in Eq. (33) applies to both *ss* and *ls* necks. The corresponding neck curvatures M_{ss}, and M_{ls} now satisfy the inequalities

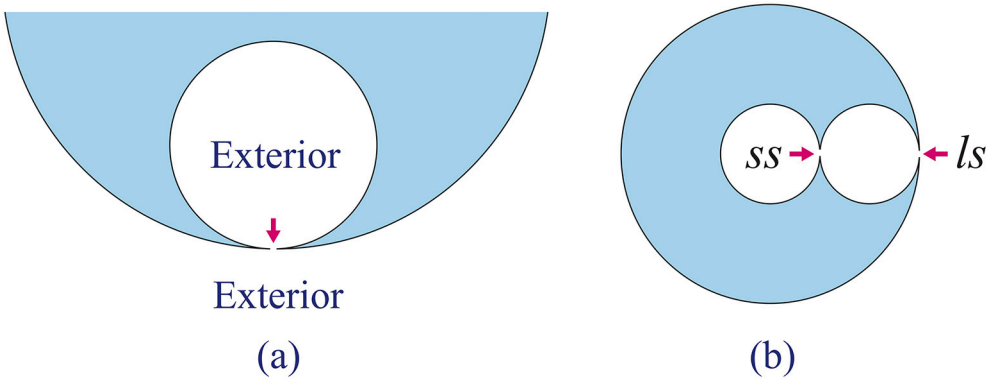

Fig. 12. Exterior necks of multispherical shapes formed by membranes with negative spontaneous curvature: (a) Exterior membrane neck (red arrow) which connects two exterior aqueous compartments (white); and (b) A (1 + 2)-multisphere consisting of one large and two small spheres connected by two types of exterior necks (two red arrows), an *ls* neck between the large and one of the small, inverted spheres, and an *ss* neck between the two small, inverted spheres.The large (punctured) sphere has positive mean curvature whereas the two small spheres have negative mean curvature. (For interpretation of the references to color in this figure legend, the reader is referred to the web version of this article.)

$M_{ss} \leq M_{ls} \leq 0$. As a consequence, both types of necks are closed if the negative spontaneous curvature satisfies

$$m \leq M_{\rm ss} \leq M_{\rm ls} \leq 0 \quad \text{(all exterior necks stably closed)} \tag{34}$$

whereas all necks are unstable against neck opening for

$$M_{\rm ss} \leq M_{\rm ls} \leq m \leq 0 \quad \text{(all exterior necks open up)}. \tag{35}$$

5.5. No multispheres with both interior and exterior necks

The stability conditions for closed necks imply that a stable multispherical shape cannot involve both interior and exterior necks. Indeed, the stability relations for interior necks is described by Eq. (28) which has the form

$$0 < M_{\rm ll} \leq M_{\rm ls} \leq M_{\rm ss} \leq m$$

whereas the stability relations for exterior necks are given by

$$m \leq M_{\rm ss} \leq M_{\rm ls} \leq 0$$

according to Eq. (34). Therefore, the same multispherical shape cannot involve both stable interior necks, for which the spontaneous curvature $m > 0$, and stable exterior necks, for which $m \leq 0$.

In particular, no multispheres can be formed with both a stable interior *ll* neck and a stable exterior *ls* neck because the corresponding stability conditions

$$0 < M_{\rm ll} \leq m \quad \text{and} \quad m \leq M_{\rm ls} \leq 0 \tag{36}$$

cannot be fulfilled for any value of the spontaneous curvature m. Note that these restrictions apply to membranes with a laterally uniform composition and thus laterally uniform elastic properties as considered here. If the membrane contains different intramembrane domains, corresponding to coexisting lipid phases, stable multispheres with both exterior and interior necks become possible.

5.6. Curvature-induced constriction forces

The stability relations for closed membrane necks can be derived by starting from a dumbbell shape with an open but narrow neck and parametrizing this shape by a piece-wise constant-mean-curvature surface. One such parametrization consists of two hemispheres connected by two unduloid segments that form a narrow neck of radius $R_{\rm ne}$ [67–69]. The dumbbell with a closed neck is obtained in the limit of zero neck radius $R_{\rm ne}$. The bending energy $E_{\rm be}$ of the dumbbell has the form [16,17]

$$E_{\rm be}(R_{\rm ne}) \approx E_{\rm be}(0) \pm 8\pi\kappa(m - M_{\rm ne})R_{\rm ne} \tag{37}$$

up to first order in $R_{\rm ne}$ where the plus and minus sign applies to interior and exterior necks, respectively. The closed neck is stable if the term proportional to the neck radius $R_{\rm ne}$ increases with increasing $R_{\rm ne}$ which implies $m > M_{\rm ne} > 0$ for interior necks and $m < M_{\rm ne} < 0$ for exterior necks.

The spontaneous curvature generates a constriction force f at the membrane neck which can be defined via the relation $f = \partial E_{\rm be}/\partial R_{\rm ne}$. Using the expression for the bending energy as given by Eq. (37), we then obtain the constriction forces [16,17,40]

$$f \approx 8\pi\kappa(m - M_{\rm ne}) \quad \text{for interior necks with } m > 0 \tag{38}$$

and

$$f \approx 8\pi\kappa(M_{\rm ne} - m) \quad \text{for exterior necks with } m < 0, \tag{39}$$

up to first order in the neck radius $R_{\rm ne}$. It is important to note that the constriction force f vanishes for $m = M_{\rm ne}$, corresponding to the neck closure condition, but increases linearly with the difference between the spontaneous curvature m and the neck curvature $M_{\rm ne}$.

If the constriction force f at the membrane neck becomes sufficently large, the neck is cleaved as recently demonstrated for the controlled division of giant vesicles [40]. In these experiments, the binding of His-tagged proteins to the outer leaflets of the vesicle membranes was used to fine-tune the spontaneous curvature m, compare Fig. 6a. The spontaneous curvature was controlled by the solution concentration of the proteins, which generated a constriction force f that was sufficient to divide the vesicles, even though the solution concentration remained in the nanomolar regime.

For a given value of the spontaneous curvature, the constriction force f is different for different types of necks. For positive spontaneous curvature, the neck curvatures M_{ls} and M_{ss} are positive and ordered according to $M_{ls} < M_{ss}$. It then follows from Eq. (38) that the associated constriction forces f_{ls} and f_{ss} fulfill the inequality

$$f_{\rm ls} \equiv 8\pi\kappa(m - M_{\rm ls}) > 8\pi\kappa(m - M_{\rm ss}) \equiv f_{\rm ss} \quad (m > 0). \tag{40}$$

For negative spontaneous curvature, the neck curvatures M_{ls} and M_{ss} are negative and ordered according to $M_{ss} < M_{ls}$ which implies $|M_{ls}| < |M_{ss}|$. It then follows from Eq. (39) that the corresponding constriction forces f_{ls} and f_{ss} fulfill the inequality

$$f_{\rm ls} \equiv 8\pi\kappa(M_{\rm ls} - m) > 8\pi\kappa(M_{\rm ss} - m) \equiv f_{\rm ss} \quad (m < 0). \tag{41}$$

Therefore, for both positive and negative spontaneous curvature the constriction force at an *ls* neck exceeds the constriction force at an *ss* neck.

In the above considerations, we have regarded the effective mean curvatures $M_{\rm ne}$ of the necks as basic local variables. However, these neck curvatures can be expressed in terms of the radii R_l and R_s of the large and small spheres and these radii depend implicitly on the sphere numbers N_l and N_s as well as on the overall vesicle geometry. This dependence becomes most transparent when we use rescaled radii r_l and r_s as well as the rescaled volume v as defined further below by Eqs. (45) and (46).

6. Different patterns of multispheres

For a given number of N_l large and N_s small spheres, we can distinguish different $(N_l + N_s)$-patterns that differ in the way, in which the spheres are mutually connected. One simple example are the two patterns of (1 + 2)-multispheres displayed in Fig. 1b and c. A general way to identify the different $(N_l + N_s)$-patterns is by mapping the large spheres onto blue vertices, the small spheres onto red vertices, and the membrane necks onto edges connecting the corresponding pairs of vertices. In this way, the multisphere pattern is mapped onto a graph, the vertices of which have two different colors. Patterns are distinct if they are mapped onto two-colored graphs that are not isomorphic.

One should note that the *inverse* mapping from two-colored graphs onto multisphere patterns is subject to the additional constraint that the individual spheres of the multisphere should not overlap and that the spherical membrane segments should not intersect [17]. Consider, for example, a graph consisting of 14 blue vertices, in which one central blue vertex is connected to the remaining 13 blue vertices. The corresponding (14_*)-multisphere pattern would consist of 13 large spheres connected to a central large sphere via 13 *ll* necks, but such a pattern is not possible because of the steric hindrance between the 14 large spheres. Likewise, we may consider a graph with a central red vertex connected to 12 blue vertices but the corresponding (12 + 1)-multisphere pattern with 12 *ls* necks is again impossible.

In this and the following sections, we will focus on multisphere patterns that can be obtained, at least in principle, by reducing the volume of a single large sphere with radius R_l equal to the vesicle size

$$R_{\rm ve} \equiv \sqrt{A/(4\pi)}\,, \tag{42}$$

which is defined in terms of the total area A of the vesicle membrane. Experimentally, the vesicle volume can be reduced by osmotic deflation, i.e., by increasing the osmotic pressure in the exterior solution. During such a deflation process, the area A remains unchanged. Furthermore, different $(N_l + N_s)$-patterns have the same number of large and small spheres which implies that they have the same volume. Therefore, in the following cartoons, all $(N_l + N_s)$-patterns are taken to have the same area and all patterns for fixed values of N_l and N_s are taken to have the same volume. If we increased the volume of any of these patterns by osmotic inflation, we would eventually return to the initial single sphere of radius $R_l = R_{ve}$. Furthermore, when mapped onto a two-colored graph, all multispheres that can be obtained from a single large sphere by volume reduction have a tree-like connectivity, i.e., the corresponding graph contains no cycles of vertices and edges. For such multispheres, the number of membrane necks is equal to $N_l + N_s - 1$. On the other hand, multispheres that contain cyles of spheres could be created by membrane fusion as briefly mentioned at the end.

The number of possible multisphere patterns increases strongly with both N_l and N_s. Counting the number of different patterns for large values of N_l and/or N_s is a difficult problem of combinatorics and will not be pursued here. Instead, we will illustrate the different patterns for relatively small values of both N_l and N_s. However, because of the local properties of closed membrane necks as described in the previous section, the stability of any $(N_l + N_s)$-pattern depends primarily on the presence or absence of *ss* and *ls* necks. Therefore, we can still draw general conclusions about the stability of any $(N_l + N_s)$-patterns. It is again important to distinguish the patterns for positive from those for negative spontaneous curvature, as described in the following two subsections.

6.1. Different patterns for positive spontaneous curvature

For positive spontaneous curvature, the small and large spheres can be connected by *ss*, *ls*, and/or *ll* necks, see Fig. 1. The different necks have the mean curvatures M_{ss}, M_{ls}, and M_{ll}, respectively, which are ordered according to $M_{ll} \le M_{ls} \le M_{ss}$. The stability of the whole pattern is determined by the least stable neck. We then have to distinguish three cases, corresponding to (i) patterns with at least one *ss* neck, (ii) patterns with no *ss* necks but at least one *ls* neck, and (iii) patterns with no *ss* and no *ls* necks.

If a pattern involves at least one *ss* neck, the pattern is stable provided the curvature M_{ss} of this neck satisfies the inequality

$$M_{ss} = \frac{1}{2}(M_s + M_s) = \frac{1}{R_s} \le m\,. \tag{43}$$

One example for this case is provided by the pattern $\mathcal{P}_1$ in Fig. 13a. Likewise, if a pattern has no *ss* necks but at least one *ls* neck, it is stable as long as the neck curvature M_{ls} is sufficiently small and fulfills the inequality

$$M_{ls} = \frac{1}{2}(M_l + M_s) = \frac{1}{2}\left(\frac{1}{R_l} + \frac{1}{R_s}\right) \le m\,. \tag{44}$$

One example is the pattern $\mathcal{P}_2$ in Fig. 13a. Because $M_{ls} \le M_{ss}$, the stability regime of $\mathcal{P}_2$ is larger than the stability regime of $\mathcal{P}_1$. These stability regimes can be described in a quantitative manner as will be shown further below.

Fig. 13 displays all possible patterns of (1 + 2)- and (2 + 1)-multispheres. In these two simple cases, only two different patterns have to be distinguished. All patterns consists of $N_{tot} = 3$ spheres and involve only two necks, which can be *ss*, *ls*, or *ll* necks, see Fig. 13. Optical images of GUVs that form the patterns $\mathcal{P}_1$ and $\mathcal{P}_2$ in Fig. 13 are displayed in Fig. 1b,c (for different v-values). In Fig. 14, all possible (2 + 2)-patterns are depicted. Now, we have to distinguish six different patterns which provides a simple example for the increased number of different patterns when we increase the sphere numbers N_l and/or N_s.

For fixed sphere numbers N_l and N_s, the different stability relations for the *ss*, *ls*, and *ll* necks lead to three different subsets of the $(N_l + N_s)$-patterns. The first subset is defined by those patterns that involve at least one *ss* neck. The second subset is defined by those patterns that involve no *ss* neck but at least one *ls* neck. For the (1 + 2)- and (2 + 1)-multispheres in Fig. 13, each of these two subsets contains only one pattern. For the (2 + 2)-multispheres in Fig. 14, on the other hand, the six possible (2 + 2)-patterns form two subsets, each of which consists of three different patterns.

The third subset of patterns is provided by $N^* = N_l + N_s$ equally sized spheres connected by membrane necks of the same type, denoted by **. For $N_* = 2$ and $N_* = 3$, only one such pattern can be formed as shown in Fig. 15. For $N_* \ge 4$, several patterns can be formed that differ in their connectivity and their number of junctions. The simplest example is provided by $N_* = 4$ with two distinct patterns: one pattern is provided by a linear chain of spheres without a junction, the second pattern by a branched chain with one three-way junction, see Fig. 15. Each (N_*)-pattern can be reached, for a given value of N_*, from different $(N_l + N_s)$-patterns with $N_{tot} = N_l + N_s = N_*$. The single (3 *)-pattern, for example, can be obtained by deflation of the two (1 + 2)-patterns and by deflation of the two (2 + 1)-pattern displayed in Fig. 13. In fact, the (N_*)-multispheres have the smallest possible volume of all multispheres with the same total number of spheres $N_{tot} = N_*$ as will be shown below.

6.2. Different patterns for negative spontaneous curvature

For negative spontaneous curvature, the membrane can form stable $(1 + N_s)$-patterns with N_s small spheres enclosed by one large sphere. These $(1 + N_s)$-patterns can involve only *ss* and *ls* necks but no *ll* necks. Furthermore, (N_*)-patterns with $N_* = N_l + N_s$ equally sized spheres are no longer possible, apart from the special case of (1 + 1)-multispheres consisting of two nested spheres that have the same size.

Some examples for $(1 + N_s)$-patterns are displayed in Fig. 16 for $N_s \le 3$ and in Fig. 17 for $N_s = 4$. For all values of N_s, only one pattern, which has N_s in-buds connected by *ls* necks to the large sphere, has no *ss* neck. All other patterns have at least one *ss* neck. Inspection of Figs. 16 and 17 shows that the number of $(1 + N_s)$-patterns with at least one *ss* neck increases strongly with N_s, from only one such pattern for $N_s = 2$, as displayed in Fig. 16, to six such patterns for $N_s = 4$, see Fig. 17.

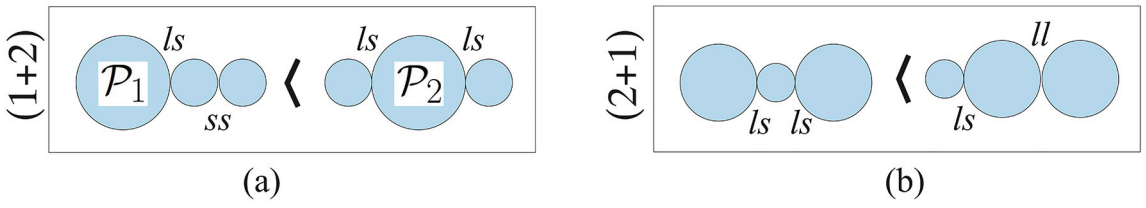

Fig. 13. (a) Two distinct patterns of (1 + 2)-multispheres: The spheres of the pattern $\mathcal{P}_1$ are connected by one *ls* and one *ss* neck whereas the pattern $\mathcal{P}_2$ with two outbuds involves only *ls* necks. Both patterns have the same vesicle volume (blue) and the same membrane area, but differ in the number of *ss* and *ls* necks. The ⟨ symbol indicates that the stability regime of the $\mathcal{P}_1$ pattern is reduced compared to the one of the $\mathcal{P}_2$ pattern; and (b) Two distinct patterns for (2+1)-multispheres with the same volume and the same area but different necks. Both in (a) and (b), the large-sphere radius is taken to be two times larger than the small-sphere radius.

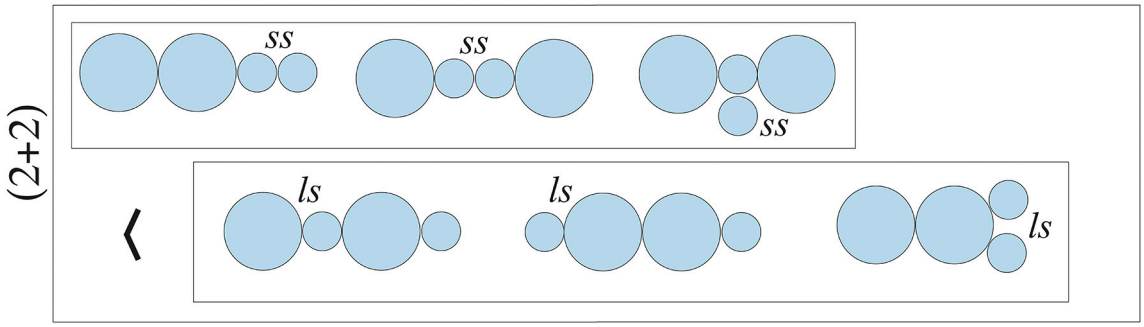

Fig. 14. Six distinct patterns of $(2 + 2)$-multispheres: For the three patterns in the top row, the least stable neck is provided by the *ss* neck. In contrast, for the three patterns in the bottom row, the *ls* neck is the least stable one. All six patterns have the same vesicle volume (blue) and the same membrane area. The large-sphere radius is taken to be two times larger than the small-sphere radius. The $\langle$ symbol indicates that the stability regime of the top-row patterns is reduced compared to the one of the bottom-row patterns. Optical images of GUVs that form the second pattern in the top row and the first pattern in the bottom row are displayed in Fig. 1f and g, respectively. (For interpretation of the references to color in this figure legend, the reader is referred to the web version of this article.)

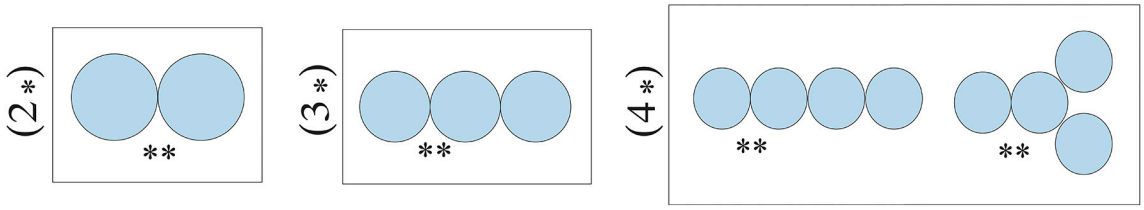

Fig. 15. Multisphere patterns of $N_* = N_l + N_s$ equally sized spheres for positive spontaneous curvature with $N_* = 2$, 3, and 4: One (2*)-pattern and one (3*)-pattern but two (4*)-patterns that differ in their connectivity: one (4*)-pattern corresponds to a linear chain without any junction, the other (4 *)-pattern is provided by a branched chain with one three-way junction. All four pattern have the same vesicle volume (blue) and the same membrane area. (For interpretation of the references to color in this figure legend, the reader is referred to the web version of this article.)

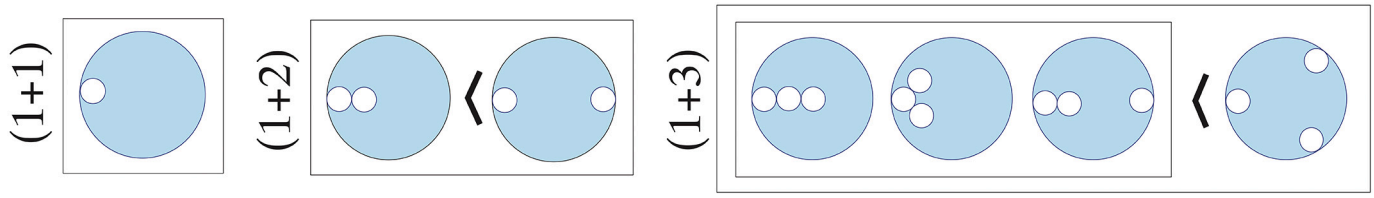

Fig. 16. $(1 + N_s)$-multisphere patterns for negative spontaneous curvature with $N_s = 1$, 2, and 3: one $(1 + 1)$-pattern; two $(1 + 2)$-patterns; and four $(1 + 3)$-patterns. For all values of N_s, only one pattern involves no *ss* neck. All patterns shown here have the same vesicle volume (blue) and the same membrane area. The large-sphere radius is taken to be five times larger than the small-sphere radius. (For interpretation of the references to color in this figure legend, the reader is referred to the web version of this article.)

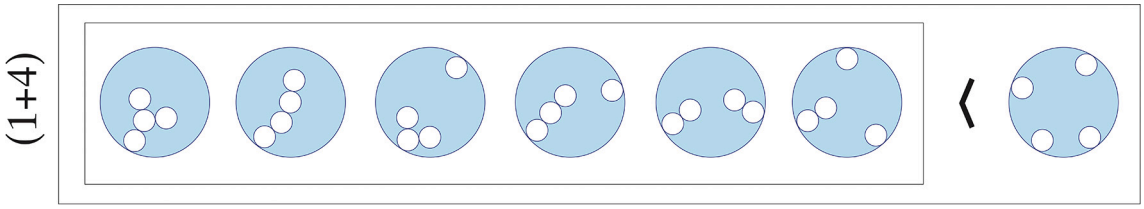

Fig. 17. Seven $(1 + 4)$-multisphere patterns for negative spontaneous curvature: Only the right-most pattern with four in-buds has no *ss* neck. Each of the other six patterns involves at least one *ss* neck, which determines their stability. All patterns have the same vesicle volume (blue) and the same membrane area. The large-sphere radius is taken to be five times larger than the small-sphere radius. (For interpretation of the references to color in this figure legend, the reader is referred to the web version of this article.)

6.3. Transmutations between different patterns

The experimental observations revealed that the small spheres are rather mobile and can be rearranged by diffusion of the *ss* necks between two small spheres [13]. In this way, a given multisphere pattern can be transmuted into another multisphere pattern, built up from the same numbers of large and small spheres. Frequent transmutations were observed for tubules of small spheres, both for the $(1 + N_s)$-multispheres in Fig. 9 and for the $(N *)$-multispheres in Fig. 8, which underwent transitions between linear and branched tubules. During these transitions, one small sphere diffused along another small sphere, corresponding to the diffusion of an *ss* neck, until this neck was transferred onto a third small sphere, thereby generating a three-way junction between four small spheres. This mobility of the small spheres provides

strong evidence that the closed membrane necks were not clamped by attractive interactions between the adjacent membrane segments.

The diffusion of a small sphere along a large sphere, corresponding to the diffusion of an *ls* neck, should also occur frequently because this diffusion process is not expected to encounter any energy barrier. What is less obvious is that a diffusing *ls* neck can be transferred onto a second small sphere which is also connected to the large sphere. Such a transfer would change the *ls* neck into an *ss* neck which may involve a substantial energy barrier. As an example, let us consider the two $(1 + 2)$-multisphere patterns, $\mathcal{P}_1$ and $\mathcal{P}_2$, in Fig. 13. The pattern $\mathcal{P}_1$ on the left involves one *ls* and one *ss* neck whereas the pattern $\mathcal{P}_2$ on the right involves two *ls* necks. Both patterns have been observed for giant vesicles, see the optical images in Fig. 1b and c. To transmute the $\mathcal{P}_2$ pattern into the $\mathcal{P}_1$ pattern, one *ls* neck must first diffuse over the membrane of the large sphere until the two small spheres are close together. In a second step, the *ls* neck can then be transferred onto the second small sphere, thereby transforming the *ls* neck into an *ss* neck.

As indicated by the $\langle$ symbol in the $(1 + 2)$-box of Fig. 13, the stability regime for the $\mathcal{P}_2$ pattern is larger than the one for the $\mathcal{P}_1$ pattern. Therefore, if $\mathcal{P}_1$ is transmuted to $\mathcal{P}_2$ for fixed shape parameters, the resulting $\mathcal{P}_2$ pattern should be stable as well. In contrast, if $\mathcal{P}_2$ is transmuted to $\mathcal{P}_1$, the resulting pattern $\mathcal{P}_1$ need not to be stable and the least stable neck will open up if the initial $\mathcal{P}_2$ pattern was located outside of the stability regime for $\mathcal{P}_1$.

6.4. Junctions of multispherical tubules

The multispherical tubules in Fig. 9 and in most panels of Fig. 8 contain multispherical junctions, corresponding to individual spheres that are connected to more than two neighboring spheres. A detailed analysis of the corresponding time-lapse movies [13] shows that most of these junctions are three-way junctions, with some exceptions, such as the junction in Fig. 8c which represents a four-way junction.

Stable three-way junctions are typical for the nanotubular network of the endoplasmic reticulum whereas stable four-way junctions seem to be quite rare [70–74] As far as membrane elasticity is concerned, there are two main differences between the multispherical tubules formed by giant vesicles as discussed here and the membrane nanotubes of the reticular networks. First, the tubules displayed in Figs. 9 and 8 have a diameter of about two micrometers whereas the nanotubes of the reticular networks have a diameter of about 50 to 100 nm, as estimated from electron microscopy images. Therefore, the membranes of the reticular networks have a much larger spontaneous curvature. Second, the tubules formed by the giant vesicles undergo strong bending fluctuations in response to thermal noise. In contrast, the tubular segments between two junctions of the reticular networks appear to be rather straight, indicating the presence of a substantial membrane tension.

To get some insight into this difference in the tubular morphology, let us consider a three-way junction as in Fig. 9a and imagine that it involves a much larger number of small spheres. The junction contains a specific small sphere, which forms the junctional center. This center is linked via three *ss* necks to three linear tubules or junctional arms. Two of these arms have a free end while one arm is connected to the large sphere via an *ls* neck. The free ends undergo strong thermal fluctuations whereas the *ls* end is constrained to move on the surface of the large sphere. We will now perform some thought experiments with this junction.

First, we aspirate the large sphere by a micropipette and grap one of the free ends by a laser trap to exert a pulling force on it. We will then encounter several distinct force regimes. First, we will straighten two arms of the junction until the pulled free end becomes colinear with the junctional center and the *ls* end. At this point, the third junctional arm will still undergo strong thermal fluctuations. When we further increase the pulling force, the small spheres of this third arm will be drawn into the straightened tube segment until all small spheres are part of this segment. When we continue to increase the pulling force even further, we may start to open up the closed necks between the small spheres. As a result, the multispherical tubule will be transformed into an unduloidal or cylindrical tubule [75]. Because of the constriction force f as given by Eq. (38), which acts to compress the closed neck, the opening of the closed membrane necks is expected to require a pulling force that exceeds a certain threshold value.

Alternatively, we may use two laser traps to exert pulling forces on the free ends of the three-way junction. These two pulling forces will act to straighten all three arms simultaneously. At the same time, the applied forces will be transmitted to the junctional center and the three arms will exert three forces onto this center. These three forces will initially be unbalanced and add up to a nonzero force acting on the center. The junction will then start to move until the three forces acting on the center add up to zero force. This force balance implies that the junctional arms form contact angles of $360/3 = 120$ degrees at the junctional center, see Fig. 18a. The latter contact angle is also observed for the reticular networks of nanotubes.

Now, let us extend these considerations to a four-way junction, again consisting of a large number of spheres. The junction is assumed to experience a significant membrane tension which leads to four straight arms of the junction. Force balance now implies that the contact angle between two neighboring arms is equal to $360/4 = 90$ degrees as in Fig. 18b. The membrane tension contributes an elastic energy that is proportional to the total length of the junctional arms. Because the membrane tubules of the four-way junction are fluid, this junction can be divided up into two three-way junctions, each of which with contact angles of 120 degrees, see Fig. 18c. It turns out that the total length of the tubules with two three-way junctions is smaller than the total length of the four-way junction which implies that the mechanical membrane tension and the membrane's elastic energy are reduced when we transform the four-way junction into two three-way junctions. This transformation is intimately related to Steiner minimal trees [76–79] as studied in mathematical graph theory.

6.5. Digression: Steiner minimal trees

In general, Steiner minimal trees are networks of vertices and edges which are connected in such a way that the total length of the edges attains the smallest possible value. The analysis of such networks has a long history [80]. The classic example are planar networks in two dimensions, built up from vertices that are connected by straight line segments. The corresponding Steiner minimal trees are relevant for many real-life applications such as the planning of road networks, canal systems, and power grids as well as the design of electric circuits and microchips.

Thus, consider N points or 'terminals' in the plane and look for a network of minimal total length interconnecting these terminals. If we impose the restriction that these terminals should be directly connected by straight line segments, we obtain a minimal spanning tree. On the other hand, if we relax this restriction and allow n additional points, so-called Steiner points, to be added to the network, the resulting network of $N + n$ vertices represents a Steiner tree. When the number n of Steiner points is varied, the Steiner tree with the shortest length defines a Steiner minimal tree. In a Steiner minimal tree, all Steiner points are connected to three other points by three edges and these three edges form mutual contact angles of 120° [76,79].

The search for Steiner minimal trees in two dimensions can be performed in the lab using soap films between two parallel glass plates that are separated by immobile posts between the plates [77,81,82]. The confinement between the plates forces the soap film to form a two-dimensional network. The terminals are provided by the posts between the plates. The fluidity of the soap film allows this film to split up, thereby creating additional Steiner points. The equilibrium state of the soap film corresponds to a minimum of its area and, thus, of its interfacial free energy, both of which are proportional to the length of the network.

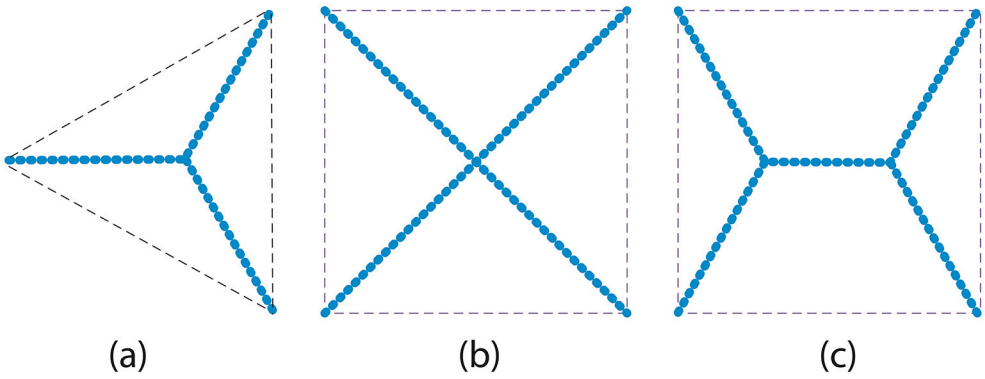

Fig. 18. Junctions of membrane tubules. Because the tubules are fluid, force balance at such a junction implies that all contact angles between neighboring tubules have the same value: (a) Three-way junction with all contact angles equal to 120°; (b) Four-way junction with all contact angles equal to 90°; and (c) Two three-way junctions with all contact angles equal to 120°. The total length of the tubules in (b) is somewhat larger than the total length of the tubules in (c), which implies a reduction in the elastic membrane energy when we transform the four-way junction in (b) into two three-way junctions. as in (c).

In practise, the soap film method is only feasible for relatively small numbers of terminals. For larger terminal numbers, the search for Steiner minimal trees requires numerical algorithms by which one can generate and compare large numbers of different Steiner trees. Even though this problem is computationally complex and known to be $\mathcal{NP}$-hard [79,83], effective algorithms have been developed to find Steiner minimal trees in two dimensions starting from minimal spanning trees [84]. The problem of finding Steiner minimal trees in three dimensions has also been addressed, in particular when the terminals form the vertices of simple polyhedra [76,78,85]. For the latter geometries, the Steiner points have the same geometric properties as in two dimensions, i.e., they are connected to three other points and the corresponding edges form mutual contact angles of 120°.

7. Geometry of multispheres

As explained previously, GUV membranes with positive spontaneous curvature form $(N_l + N_s)$-multispheres, consisting of N_l large spheres with radius R_l and N_s small spheres with radius R_s, see Fig. 1. In contrast, GUV membranes with negative spontaneous curvature form $1 + N_s$ multispheres, consisting of one large sphere with radius R_l and N_s small, inverted spheres with radius R_s, see Fig. 2. In both cases, the geometry of the multispheres is described by two relatively simple geometric relations that will be examined in the present section. In contrast to the local properties discussed in Sections 4 and 5, the two geometric relations are global in the sense that they depend explicitly on the sphere numbers N_l and N_s.

7.1. Dimensionless shape parameters

It will be useful to perform the following analysis using dimensionless quantities. The vesicle size $R_{\rm ve} = \sqrt{A/(4\pi)}$ as defined in Eq. (42) is taken to provide the basic length scale and all radii will be measured in units of $R_{\rm ve}$. We then obtain the dimensionless radii

$$r_l \equiv \frac{R_l}{R_{\rm ve}} \quad \text{and} \quad r_s \equiv \frac{R_s}{R_{\rm ve}} \tag{45}$$

for the large and small spheres.

Another important quantity that will enter the geometric relations is the rescaled volume v, which is defined by dividing the vesicle volume V by the volume of a sphere with radius $R_{\rm ve}$, i.e., by

$$v \equiv \frac{V}{\frac{4\pi}{3}R_{\rm ve}^3} \quad \text{with}\, 0 < v \le 1. \tag{46}$$

For fixed membrane area A and thus fixed vesicle size $R_{\rm ve}$, the lower boundary value $v = 0$ corresponds to a vesicle with vanishing volume whereas the upper boundary value $v = 1$ corresponds to a single large sphere.

7.2. Multisphere geometry for positive spontaneous curvature

A multisphere consisting of N_l large spheres of radius R_l and N_s small spheres of radius R_s has the surface area

$$A = 4\pi\big(N_l R_l^2 + N_s R_s^2\big) \tag{47}$$

and the volume

$$V = \frac{4\pi}{3}\big(N_l R_l^3 + N_s R_s^3\big)\,. \tag{48}$$

When expressed in terms of the dimensionless parameters, the area relation in Eq. (47) becomes

$$N_l r_l^2 + N_s r_s^2 = 1 \tag{49}$$

and the volume relation in Eq. (48) attains the simple form

$$N_l r_l^3 + N_s r_s^3 = v\,, \tag{50}$$

with the rescaled volume v as defined in Eq. (46). Therefore, for $m > 0$, we obtain two equations for the two variables r_l and r_s, which depend on three parameters as provided by the large-sphere number N_l, the small-sphere number N_s, and the rescaled volume v.

7.2.1. Multispheres consisting of equally sized spheres

In order to understand the possible solutions of the two geometric relationships in Eqs. (49) and (50), we first consider the limiting case of $N_l + N_s = N_*$ equally sized spheres with rescaled radius $r_l = r_s \equiv r_*$. The area relation in Eq. (49) then simplifies and becomes

$$(N_l + N_s) r_*^2 = 1\,. \tag{51}$$

This equation has one positive and one negative root for r_*. To be physically meaningful, the radius r_* must we positive. Thus, we discard the negative root and obtain the single solution

$$r_* = \frac{1}{\sqrt{N_l + N_s}} > 0\,. \tag{52}$$

Furthermore, for $r_l = r_s = r_*$, the volume relation in Eq. (50) implies

$$v = (N_l + N_s) r_*^3 = \frac{1}{\sqrt{N_l + N_s}} \equiv v_* \tag{53}$$

where the second equality is obtained by inserting the explicit expression $r_* = 1/\sqrt{N_l + N_s}$. As shown further below, the volume $v = v_*$ corresponds to a boundary minimum of the volume v as a function of the radius r_s.

The geometric relations in Eqs. (49) and (50) lead to a single solution for $N_l + N_s$ equally sized spheres with radius $r = r_*$ and volume $v = v_*$ as given by Eqs. (52) and (53). As a consequence, the condition that the small-sphere radius r_s should not exceed the large-sphere radius r_l can

now be divided up into two separate conditions as provided by

$$0 \le r_s \le r_* \quad \text{for the small-scale radius } r_s \tag{54}$$

and by

$$r_* \le r_l \le 1 \quad \text{for the large-scale radius } r_l. \tag{55}$$

7.2.2. Large-sphere radius as a function of small-sphere radius

In the following, we will regard the small-sphere radius r_s as the independent variable which implies that the large-sphere radius r_l becomes a function of r_s. Indeed, the area relation in Eq. (49) then leads to

$$r_l = \frac{1}{\sqrt{N_l}} \sqrt{1 - N_s r_s^2} \equiv g(r_s) \tag{56}$$

where the positive root of r_l^2 was chosen in order to implement the physical requirement that the radius r_l must be positive. Furthermore, the discriminant under the square root in Eq. (56) is positive or zero for all r_s-values within the range $0 \le r_s \le r_*$ as given by Eq. (54) because $r_* \le 1/N_s$.

The boundary values of $g(r_s)$ as obtained for $r_s = 0$ and $r_s = r_*$ are

$$r_l = g(0) = \frac{1}{\sqrt{N_l}} \quad \text{for } r_s = 0 \tag{57}$$

and

$$r_l = g(r_*) = \frac{1}{\sqrt{N_l}} \sqrt{1 - N_s r_*^2} = r_* \quad \text{for } r_s = r_* . \tag{58}$$

7.2.3. Dependence of volume on small-sphere radius

When we insert the expression for $r_l = g(r_s)$ as given by Eq. (56) into the volume relation in Eq. (48), we obtain the functional relationship

$$v = h(r_s) \tag{59}$$

with the volume function

$$h(r_s) \equiv \frac{1}{\sqrt{N_l}} \left(1 - N_s r_s^2\right)^{3/2} + N_s r_s^3 , \tag{60}$$

which represents the volume v as an algebraic function of the small-sphere radius r_s. The volume function $h(r_s)$ is again defined for the whole range of possible r_s-values as given by $0 \le r_s \le r_*$ and has the boundary values

$$v = h(0) = \frac{1}{\sqrt{N_l}} \quad \text{for } r_s = 0 \tag{61}$$

and

$$v = h(r_*) = \frac{1}{\sqrt{N_l + N_s}} = v_* \quad \text{for } r_s = r_* . \tag{62}$$

7.2.4. Local extrema of volume function

Next, we determine those values of r_s for which the volume function $h(r_s)$ attains a local extremum, i.e., at which the first derivative of h with respect to r_s vanishes. Using the explicit expression for the volume function h as given by Equ (60), this derivative becomes

$$\frac{\mathrm{d}h}{\mathrm{d}r_s} = 3N_s r_s (r_s - r_l) \quad \text{with} \quad r_l = g(r_s) \tag{63}$$

as in Eq. (56). This expression vanishes for two different values of r_s. First, it vanishes for

$$r_s = 0 \quad \text{with} \quad v = h(r_s = 0) = \frac{1}{\sqrt{N_l}} \tag{64}$$

and the large-sphere radius $r_l = 1/\sqrt{N_l}$. The volume function $h(r_s)$ attains a *local maximum* at $r_s = 0$ because

$$\frac{\mathrm{d}^2 h}{\mathrm{d}r_s^2}\Big|_{r_s=0} = -\frac{3N_s}{\sqrt{N_l}} < 0 . \tag{65}$$

Second, the first derivative of the volume function h also vanishes for

$$r_l = r_s = r_* = \frac{1}{\sqrt{N_l + N_s}} , \tag{66}$$

corresponding to the radius r_* of $N_l + N_s$ equally sized spheres. At $r_s = r_*$, the volume function $h(r_s)$ attains a *local minimum* because

$$\frac{\mathrm{d}^2 h}{\mathrm{d}r_s^2}\Big|_{r_s=r_*} = \frac{3N_s}{N_l} \sqrt{N_l + N_s} > 0 . \tag{67}$$

7.2.5. General features of volume function

As shown above, the volume function $v = h(r_s)$ has only two local extrema, a local maximum at $r_s = 0$, where it attains the value $v = h(0) = 1/\sqrt{N_l}$ as in Eq. (61), and a local minimum at $r_s = r_*$ with $v = h(r_*) = 1/\sqrt{N_l + N_s}$ as in Eq. (62). As a consequence, the function $v = h(r_s)$ decreases monotonically from its maximum at $r_s = 0$ to its minimum at $r_s = r_*$.

The dependence of the volume v on the small-sphere radius r_s is displayed in Fig. 19 for $(N_l + N_s)$-multispheres with $N_l = 1$ as well as $N_s = 2$, 3, and 15 small spheres. Because these multispheres involve only one large sphere, all volume functions have the maximal value $v(0) = 1/\sqrt{N_l} = 1$. Note that the range of possible v-values, as given by $v_* \le v \le 1$ increases with the small-sphere number N_s because $v_* = 1/\sqrt{N_l + N_s}$ decreases with increasing N_s. Optical images for the $(1 + N_s)$-multispheres chosen in Fig. 19 are displayed in Fig. 1b,e and in Fig. 9b.

For $(N_l + N_s)$-multispheres with $N_l \ge 2$, the volume function attains the maximal value $v = h(0) = 1/\sqrt{N_l} \le 1/\sqrt{2}$ and then decreases monotonically towards its minimal value $v_* = 1/\sqrt{N_l + N_s}$.

7.2.6. Volume regimes for positive spontaneous curvature

In the general case of $(N_l + N_s)$-multispheres, we need to distinguish up to four different volume regimes. First, the formation of multispheres consisting of a total number of $N_{\mathrm{tot}} = N_l + N_s$ spheres is impossible for small values of v with

$$v < v_* = \frac{1}{\sqrt{N_l + N_s}} = \frac{1}{\sqrt{N_{\mathrm{tot}}}} \quad \text{(no multispheres)}. \tag{68}$$

This conclusion is valid irrespective of the values of the small- and large-sphere radii. Second, the degenerate case of $N_{\mathrm{tot}} = N_*$ equally sized spheres is only possible for the volume

$$v = v_* = \frac{1}{\sqrt{N_l + N_s}} = \frac{1}{\sqrt{N_*}} \quad \text{(equally sized spheres)}, \tag{69}$$

corresponding to the smallest possible volume of all $(N_l + N_s)$-multispheres with $N_l + N_s = N_*$, see the examples in Fig. 19. It is interesting to note that the minimal volume v_* decreases with increasing total sphere number $N_l + N_s$.

Third, the formation of an $(N_l + N_s)$-multisphere is possible if the volume lies within the range

$$v_* < v \le \frac{1}{\sqrt{N_l}} \quad \text{(multisphere with } r_s < r_l), \tag{70}$$

where the maximal volume $v = 1/\sqrt{N_l}$ is obtained for the small-sphere radius $r_s = 0$. Fourth, no multisphere can be formed for the volume range

$$\frac{1}{\sqrt{N_l}} < v \le 1 \quad \text{(no multispheres)}. \tag{71}$$

For multispheres with $N_l = 1$ as considered in Fig. 19, the latter volume regime is absent and the third regime as described by Eq. (70) extends up to $v = 1$.

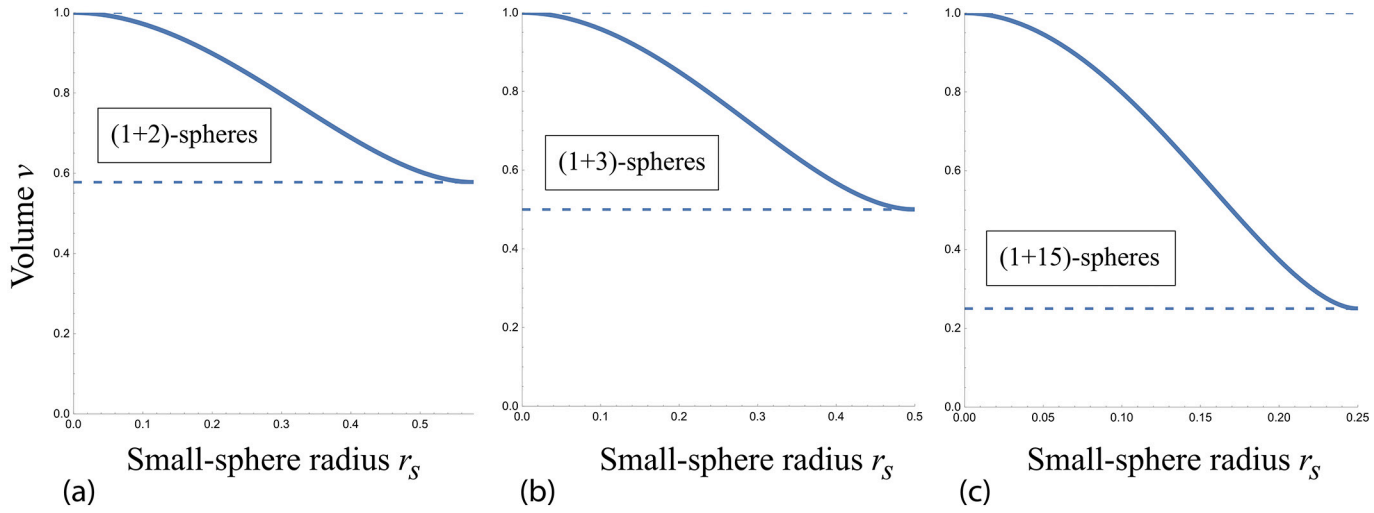

Fig. 19. Volume v as a function of small-sphere radius r_s for $(1 + N_s)$-multispheres with positive spontaneous curvature: (a–c) Volume functions as described by Eq. (60) (a) for $N_s = 2$ as in Fig. 1b; (b) for $N_s = 3$ as in Fig. 1e; and (c) for $N_s = 15$ as in Fig. 9b. The upper dashed lines are located at $v = 1/\sqrt{N_l} = 1$ which represents the largest possible volume of the multisphere. The lower dashed lines are located at $v = v_* = 1/\sqrt{N_l + N_s}$, corresponding to $N_l + N_s$ equally sized spheres and the smallest possible volume.

7.3. Multisphere geometry for negative spontaneous curvature

For negative spontaneous curvature, $m < 0$, the geometric relationships simplify because the multispheres can involve only one large sphere, that is, the large-sphere number $N_l = 1$. Indeed, if two large spheres with positive mean curvature are connected by a closed *ll* neck, the corresponding neck curvature satisfies $0 < M_{ll} \le m$ as in Eq. (28), which cannot be fulfilled if the spontaneous curvature m is negative, compare Eq. (36).

The area of a $(1 + N_s)$-multisphere with N_s small, inverted spheres is given by

$$A = 4\pi\left(R_l^2 + N_s R_s^2\right) \tag{72}$$

and its volume by

$$V = \frac{4\pi}{3}\left(R_l^3 - N_s R_s^3\right). \tag{73}$$

The minus sign in front of the second term reflects the fact that V describes the volume of the interior solution whereas all small spheres are filled with exterior solution, see the small spheres (white) in Figs. 12, 16, and 17. When expressed in terms of the dimensionless radii r_l and r_s as defined by Eq. (45), the area relation in Eq. (72) becomes

$$r_l^2 + N_s r_s^2 = 1 \tag{74}$$

and the volume relation in Eq. (73) attains the form

$$r_l^3 - N_s r_s^3 = v\,, \tag{75}$$

with the rescaled volume v as in Eq. (48). Therefore, for $m < 0$, we obtain two equations for the two variables r_l and r_s which depend on only two parameters, the small-sphere number N_s and the rescaled volume v.

7.3.1. Dependence of volume on small sphere radius

Next, we use the area relationship in Eq. (74) to express the large sphere radius r_l as a function of the small sphere radius r_s. Because the large sphere radius must be positive, we take the positive root of r_l^2 in Eq. (74) which leads to

$$r_l = \sqrt{1 - N_s r_s^2}\,. \tag{76}$$

The physical requirement that the large sphere radius r_l as given by Eq. (76) should be real-valued implies that the values of the small sphere radius r_s must be restricted to the range $0 \le r_s \le 1/\sqrt{N_s}$.

Inserting the expression for the large scale radius r_l in Eq. (76) into the volume relation as given by Eq. (75), we obtain the functional dependence of the volume v on the small sphere radius r_s which has the form

$$v = \left(1 - N_s r_s^2\right)^{3/2} - N_s r_s^3\,. \tag{77}$$

To determine the physically meaningful range of the small sphere radius r_s, we impose two additional constraints. First, we require that the volume should not be negative, that is, $v \ge 0$. The condition $v = 0$ is equivalent to

$$\left(1 - N_s r_s^2\right)^{1/2} = N_s^{1/3} r_s \quad \text{or} \quad r_s = \frac{1}{\sqrt{N_s + N_s^{2/3}}}\,. \tag{78}$$

Therefore, the volume v as given by Eq. (77) satisfies

$$v \ge 0 \quad \text{for} \quad 0 \le r_s \le \frac{1}{\sqrt{N_s + N_s^{2/3}}}\,. \tag{79}$$

This upper boundary value for r_s is smaller than $1/\sqrt{N_s}$ and, thus, reduces the range of physically meaningful r_s-values as previously obtained from the requirement that the large sphere radius r_l in Eq. (76) must be real-valued. This range of r_s-values is further reduced by the additional constraint that the individual spheres of the $(1 + N_s)$-multispheres must not overlap with each other or, equivalently, that the membrane that forms the multispherical shape must not intersect itself. Thus, for each value of N_s, we need to determine the largest value of r_s, at which the spheres come into contact and start to touch each other.

This touching condition is depicted in Fig. 20 for three examples corresponding to $(1 + N_s)$-multispheres with $N_s = 2$, 3, and 13. The numerical values of the different quantities that characterise the resulting close packing of the small spheres are given in Table 1. Inspection of this table shows that both radii r_l and r_s decrease, reflecting the conserved membrane area, whereas the ratio r_l/r_s increases with increasing N_s. Furthermore, the close packing volume v_{cp}, for which all spheres touch each other, decreases with N_s. The overall dependence of the volume v on the small sphere radius r_s is displayed in Fig. 21, where the close packing volumes are included as horizontal dashed lines.

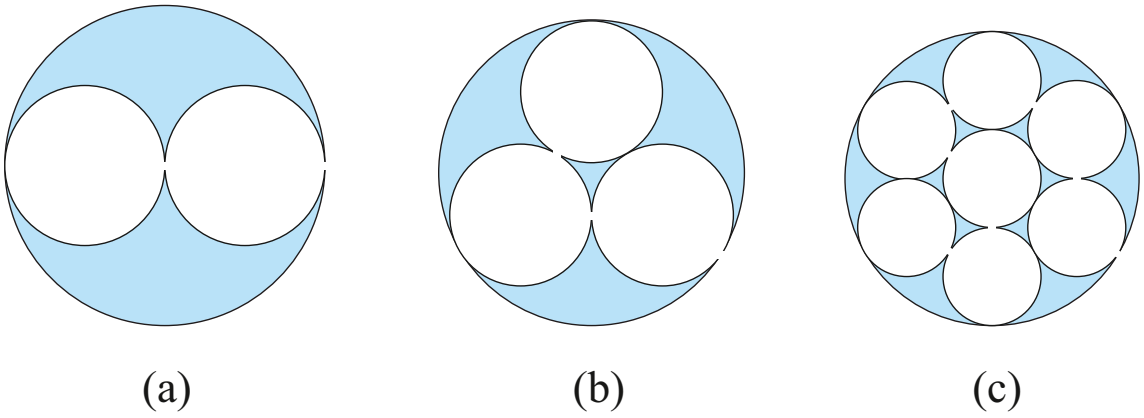

Fig. 20. $(1 + N_s)$-spheres for negative spontaneous curvature with N_s closed-packed small spheres: (a–c) Close packing for $N_s = 2$, 3, and 13 small spheres within the large sphere. In (c), only the small spheres that lie in the equatorial cross-section are displayed. In all three panels, the membranes forming the $(1 + N_s)$-sphere have the same surface area, whereas the volume $v = v_{cp}$ of the interior solution (blue) decreases from (a) to (c). The exterior solution is shown in white. The numerical values of the associated geometric parameters are provided in Table 1.

Table 1
$(1 + N_s)$-multispheres with negative spontaneous curvature, close packing of N_s small spheres within one large sphere: Numerical values of small-sphere radius r_s, large-sphere radius r_l, ratio r_l/r_s, close packing volume v_{cp}, and close packing density Φ_{cp} as defined in Eq. (81). All quantities are dimensionless.

N_s	1	2	3	4	13
r_s	0.7071	0.4082	0.3617	0.3343	0.2132
r_l	0.7071	0.8165	0.7794	0.7437	0.6396
r_l/r_s	1	2	2.1547	2.2247	3
v_{cp}	0	0.4082	0.3315	0.2619	0.1357
Φ_{cp}	1	0.25	0.2999	0.3633	0.4815

7.3.2. *Volume range for negative spontaneous curvature*

The previous considerations imply that a membrane with negative spontaneous curvature can form $(1 + N_s)$-multispheres when the volume v lies within the range

$$1 \geq v \geq v_{cp} \tag{80}$$

where the close packing volume v_{cp} decreases with increasing small-sphere number N_s, see Fig. 20 and Table 1.

The $(1 + N_s)$-multispheres shown in Fig. 2 are formed by the growth of inward-pointing membrane protrusions into tubules of small spheres. During such a process, the small spheres are likely to experience the confinement by the membrane of the large sphere as soon as the length of the small-sphere tubule becomes large compared to the diameter of the large sphere. However, the multispherical membrane is fluid and the tubule of small spheres is quite flexible. As a consequence, the tubule undergoes strong thermally-excited undulations for which the membrane necks act as flexible hinges. In addition, the multispherical tubule can further relax the steric constraint arising from the large sphere by forming a branched chain as in Fig. 9c.

7.4. *Digression: close packing of identical spheres*

The close packing density Φ_{cp}, which has been included in Table 1, is equal to the fraction of the combined volume, $N_s \frac{4\pi}{3} R_s^3$, of all small spheres to the volume $\frac{4\pi}{3} R_l^3$ of the large sphere which implies

$$\Phi_{cp} \equiv \frac{N_s R_s^3}{R_l^3} = \frac{N_s r_s^3}{r_l^3} \,. \tag{81}$$

The close packing density of identical spheres has attracted the curiosity of scientists ever since 1611, when Johannes Kepler wrote a booklet on "The Six-Cornered Snowflake" [86]. In this booklet, he

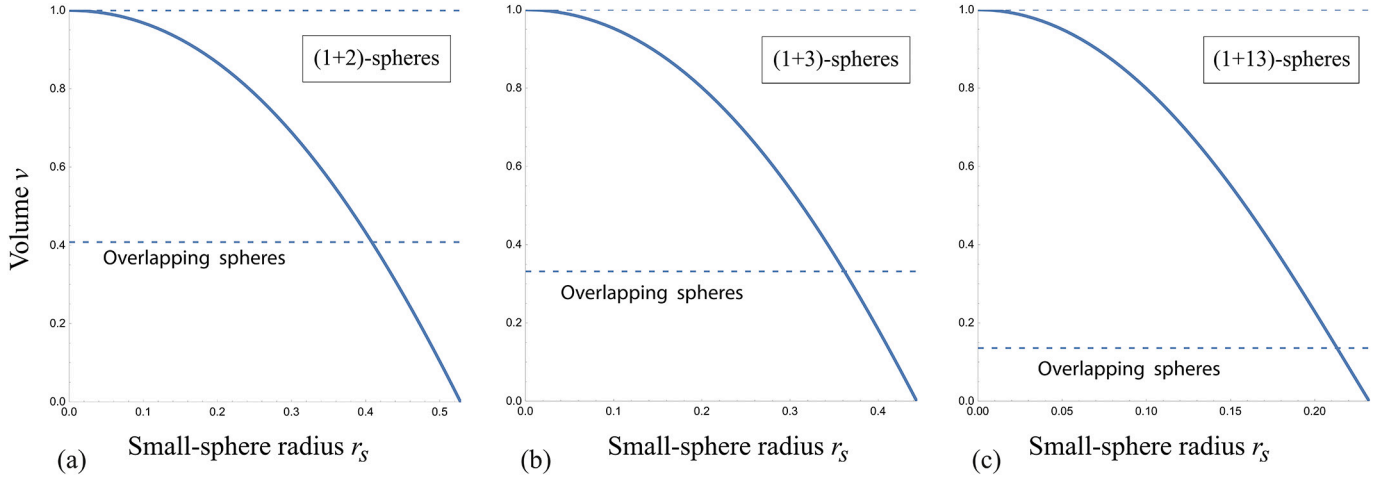

Fig. 21. Volume v as a function of the small-sphere radius r_s for negative spontaneous curvature, as described by Eq. (77): Functional dependence of v for $(1 + 2)$-multispheres in (a), for $(1 + 3)$-multispheres in (b), and for $(1 + 13)$-multispheres in (c). In each panel, the lower dashed line corresponds to the close packing volume $v = v_{cp}$, at which all spheres start to touch each other, see Fig. 9. For $v < v_{cp}$, the spheres overlap and the multispherical membrane intersects itself. The numerical values for v_{cp} are included in Table 1.

hypothesized that the hexagonal shapes of snowflakes might arise from the close packing of identical spherical 'ice particles'. In addition, he also proposed, without proof, that the densest possible packing of such identical spheres in three dimensions is provided by what we now know as the regular close packing of spheres on a face-centered cubic lattice. The corresponding packing density is equal to

$$max[\Phi_{cp}] = \frac{\pi}{3\sqrt{2}} = 0.7405\,. \tag{82}$$

The mathematical proof of this apparently simple statement, which became to be known as Kepler's conjecture, turned out to be rather difficult. Such a proof has not been found until quite recently. Indeed, a complex computer-aided proof has been announced in 1998 and was finally published in 2006 [87,88]. The delay in publication was caused by the difficulties that the referees had in verifying the proof [89].

The value of the packing density in Eq. (81) also corresponds to the widely used packing of spherical objects such as oranges or cannonballs, provided one focusses on the inner spheres, which are in contact with twelve nearest-neighbor spheres. If the spheres are packed into a finite container, the spheres close to the surface of this container have less nearest neighbors, which acts to reduce the packing density Φ_{cp}. Indeed, for the packing of 13 small spheres in Fig. 9c, the packing density is $\Phi_{cp} = 0.4815$, see last row of Table 1, which is quite a bit smaller than the maximal possible value max $[\Phi_{cp}] = 0.7405$ in three dimensions.

Another reason why the packing density Φ_{cp} is often reduced compared to its maximal possible value is the dynamics of the packing process. As an example, consider monodisperse spheres as a model for granular material such as sand. If one pours such a material into a container, one finds an initial packing density which is quite a bit lower than max$[\Phi_{cp}]$ but can be increased to about $\Phi_{cp} = 0.63$ to 0.64 by shaking the container in a random manner [90–92]. The resulting random close packing involves jammed clusters of spheres that prevent the local relaxation of neighboring clusters.

8. Stability regimes of multispherical shapes

We will now combine the multisphere geometry as described in the previous section with the stability conditions for closed membrane necks as given by Eqs. (27) and (33). As a result, we obtain the multisphere stability regimes within the morphology diagram, which is defined by two dimensionless shape parameters, the (rescaled) volume v as introduced in Eq. (46) and the (rescaled) spontaneous curvature

$$\overline{m} \equiv mR_{ve} \quad \text{with the vesicle size } R_{ve} = \sqrt{A/(4\pi)}. \tag{83}$$

We will also use the rescaled neck curvature $\overline{M}_{ab}$ as defined by

$$\overline{M}_{ab} \equiv M_{ab}R_{ve} = \frac{1}{2}(M_a + M_b)R_{ve} \tag{84}$$

and express the stability conditions for closed necks in terms of the rescaled variables $\overline{m}$ and $\overline{M}_{ab}$.

Another interesting feature of stable multispherical shapes is the mechanical tension Σ experienced by the vesicle membranes. The expression for the total tension Σ_{tot} in Eq. (9) leads to the mechanical membrane tension

$$\Sigma = \Sigma_{tot} - 2\kappa m^2 = 2\kappa m(M_l + M_s - m)\,. \tag{85}$$

which depends on the curvature-elastic parameters κ and m as well as on the vesicle geometry via $M_l = 1/R_l$ and $M_s = \pm 1/R_s$. Furthermore, the tension-curvature relationship in Eq. (85) does not depend explicitly on the sphere numbers N_l and N_s but only implicitly via the radii R_l and R_s of the large and small spheres, see the geometric relations in Sections 7.2 and 7.3.

In the following, we will examine the stability regimes for positive and negative spontaneous curvatures. In both cases, the stability regimes involve two boundary lines of limit shapes, which follow from the neck closure conditions for *ls* and *ss* necks. For positive spontaneous curvature, the stability regimes also involve a third boundary line of limit shapes, corresponding to N_* equally sized spheres. The latter line follows directly from the geometry of the multispheres which implies that such spheres cannot be formed when the volume v is below the threshold value $v_* = 1/\sqrt{N_l + N_s}$.

8.1. Stability regimes for positive spontaneous curvature

For positive spontaneous curvature, the membrane can form multispheres with a variable number of N_l large and N_s small spheres, see the optical images in Fig. 1 as well as the cartoons in Figs. 13 and 14. Furthermore, for given values of N_l and N_s, the multispheres can exhibit distinct $(N_l + N_s)$-patterns that differ in the way in which the spheres are mutually connected. For each pattern, the stability regime depends on the neck closure conditions for the *ss* and *ls* necks. The corresponding neck closure conditions define two boundary lines within the morphology diagram, corresponding to the limit shapes L^{ls}_{Nl+Ns} and L^{ss}_{Nl+Ns}, see red and curved blue lines in Fig. 22. A third boundary line is provided by the line of equally sized spheres, denoted by L_{N^*} and included as the horizontal blue lines in Fig. 22.

8.1.1. Equally sized spheres as limit shapes

The limit shapes L_{N^*} consist of $N_* = N_l + N_s$ equally sized spheres and have the (rescaled) volume

$$v = v_* = \frac{1}{\sqrt{N_l + N_s}} = \frac{1}{N_*}$$

as in Eq. (69). Each of the N_* spheres has the same radius given by

$$r_* = \frac{1}{\sqrt{N_l + N_s}} = \frac{1}{N_*}\,.$$

as in Eq. (66). Furthermore, each of the closed necks connecting two equally sized spheres has the rescaled neck curvature

$$\overline{M}_{**} = \frac{1}{2}\left(\frac{1}{r_*} + \frac{1}{r_*}\right) = \frac{1}{r_*}\,. \tag{86}$$

Finally, the condition for these necks to be stably closed now has the form

$$\overline{m} \geq \overline{M}_{**} = \frac{1}{r_*} = \sqrt{N_l + N_s} \equiv \overline{m}_*\,, \tag{87}$$

where the lower boundary value $\overline{m} = 1/r_*$ describes the neck closure condition. Therefore, the line of limit shapes L_{N^*} is located at

$$v = v_* = \frac{1}{\sqrt{N_l + N_s}} \quad \text{and} \quad \overline{m} \geq \overline{m}_* = \sqrt{N_l + N_s}\,. \tag{88}$$

which includes the neck closure condition $\overline{m}_* = 1/r_*$.

The location $(\overline{m}, v) = (\overline{m}_*, v_*)$ in the morphology diagram provides a special corner point at which the line of limit shapes L_{N^*} meets the other two lines of limit shapes, see Fig. 22. At this corner point, the constant mean curvature $\overline{M}_* = 1/r_* = \sqrt{N_*} = \sqrt{N_l + N_s}$ of the N_* spheres is equal to the spontaneous curvature $\overline{m} = \overline{m}_*$ as given by Eq. (87). Therefore, at the corner points, the (N_*)-multispheres provide constant-mean-curvature surfaces that satisfy the Euler–Lagrange Eq. (19) with the mean curvature M being equal to the spontaneous curvature m.

8.1.2. Limit shapes from the closure of membrane necks

The volume v of the multispherical shapes can be parametrized in terms of the small-sphere radius r_s, see Fig. 19. The same parametrization will now be used for the closure conditions of the different necks. The closure condition for *ss* necks then leads to the spontaneous

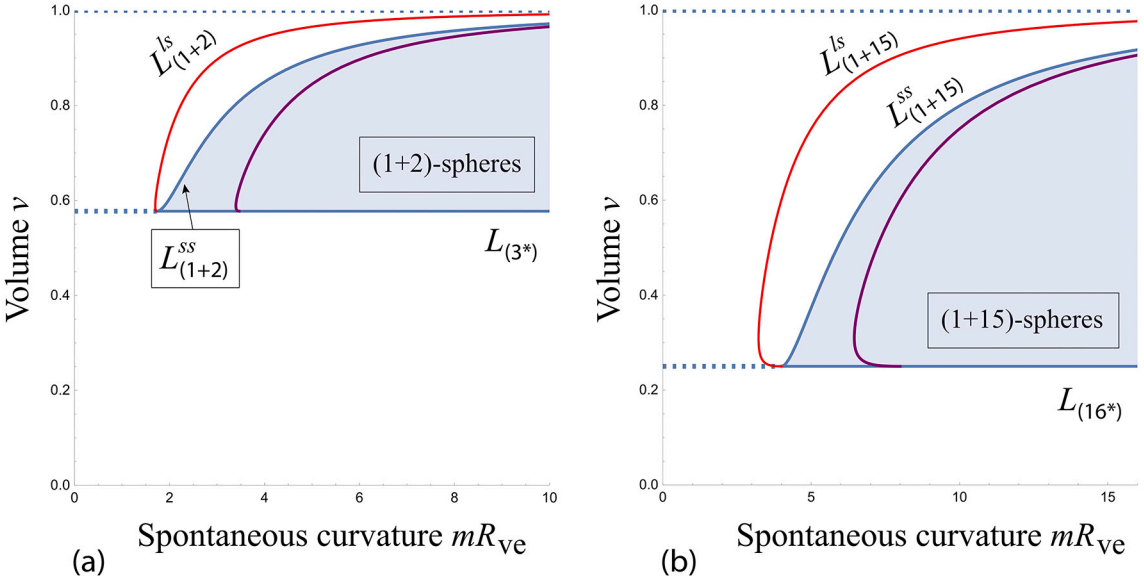

Fig. 22. Stability regimes of $(1+2)$- and $(1+15)$-multisphere patterns for positive spontaneous curvature. In both cases, the stability regime involves three boundary lines of limit shapes, denoted by L^{ls}_{Nl+Ns} (red lines), L^{ss}_{Nl+Ns} (curved blue lines), and L_{N^*} (horizontal blue lines): (a) The $(1+2)$-patterns $\mathcal{P}_1$ and $\mathcal{P}_2$, see Figs. 13a and 1b,c, lead to two somewhat different stability regimes. Both patterns are stable within the blue-shaded region. The $(1+2)$-pattern $\mathcal{P}_2$ with two out-buds is also stable within the white stripe between the curved blue and the red line; and (b) The $(1+15)$-patterns with at least one *ss* neck are stable within the blue-shaded region. The $(1+15)$-patterns with no *ss* necks and at least one *ls* neck are stable in the same region as well as in the white stripe between the curved blue line and the red line. In both (a) and (b), the mechanical tension Σ vanishes along the purple lines. (For interpretation of the references to color in this figure legend, the reader is referred to the web version of this article.)

curvature

$$\overline{m} = \overline{m}_{ss}(r_s) = \frac{1}{2}(\overline{M}_s + \overline{M}_s) = \frac{1}{r_s} \tag{89}$$

whereas the closure condition for *ls* necks becomes

$$\overline{m} = \overline{m}_{ls}(r_s) = \frac{1}{2}\left(\frac{\sqrt{N_l}}{\sqrt{1-N_s r_s^2}} + \frac{1}{r_s}\right), \tag{90}$$

where the first term represents the inverse large-sphere radius $1/r_l$. The corresponding boundary lines of limit shapes can then be obtained by parametric plots in the morphology diagram, using the volume function $v = h(r_s)$ as in Eq. (60) and the neck closure conditions in Eqs. (90) or (89) for *ls* and *ss* necks. When this method is used for $(1+2)$- and $(1+15)$-multisphere patterns, one obtains the red and curved blue lines in Fig. 22.

8.1.3. Mechanical membrane tension

The mechanical membrane tension Σ is obtained by substracting the spontaneous membrane tension $2\kappa m^2$ from the total membrane tension Σ_{tot} which leads to $\Sigma = 2\kappa m(M_l + M_s - m)$ as in Eq. (85). The mechanical tension vanishes for $m = M_l + M_s$ or for

$$\overline{m} = 2\overline{m}_{ls}(r_s) = \frac{\sqrt{N_l}}{\sqrt{1-N_s r_s^2}} + \frac{1}{r_s}\,. \tag{91}$$

Because $2\overline{m}_{ls}(r_s) > 1/r_s = \overline{m}_{ss}(r_s)$, see Eq. (89), the multispheres with vanishing mechanical tension are located within the stability regime of the $(N_l + N_s)$-patterns with at least one *ss* neck, corresponding to the purple lines within the blue-shaded regions in Fig. 22a and b.

When we keep the volume v fixed but change the spontaneous curvature $\overline{m}$ within the stability regime of the pattern, the geometry of the $(N_l + N_s)$-multisphere does not change which implies that the curvature sum $M_l + M_s$ remains unchanged as well. Therefore, the mechanical tension becomes large and negative with

$$\Sigma \approx -2\kappa m^2 \quad \text{for large positive } m. \tag{92}$$

On the other hand, using the neck closure condition $M_l + M_s = 2m$ for *ls* necks, we obtain the mechanical tension

$$\Sigma = 2\kappa m^2 > 0 \quad \text{for the limit shapes } L^{ls}_{Nl+Ns} \tag{93}$$

which are located along the red boundary lines in Fig. 22. Likewise, using the neck closure condition $M_s = m$ for *ss* necks, the mechanical tension becomes

$$\Sigma = 2\kappa m M_l > 0 \quad \text{for the limit shapes } L^{ss}_{Nl+Ns} \tag{94}$$

which are located along the curved blue lines in Fig. 22. Thus, the membranes of both limit shapes L^{ls}_{Nl+Ns} and L^{ss}_{Nl+Ns} experience a positive mechanical tension. Furthermore, in both cases, the tension Σ increases when we move along the boundary lines towards larger values of m.

For the limit shapes provided by $N_* = N_l + N_s$ equally sized spheres, the curvature sum $M_l + M_s = 2m_*$ which leads to the mechanical tension

$$\Sigma = 2\kappa m\left(\frac{2\sqrt{N_*}}{R_{ve}} - m\right) \quad \text{for the limit shapes } L_{N^*} \tag{95}$$

which are located along the horizontal blue lines in Fig. 22.

8.2. Stability regimes for negative spontaneous curvature

For negative spontaneous curvature, the membrane can form multispheres with a variable number N_s of small spheres which are enclosed in one large sphere, see the optical images in Fig. 2 as well as the cartoons in Figs. 16 and 17. Furthermore, for a given value of N_s, the multispheres exhibit distinct $(1+N_s)$-patterns that can involve *ls* and *ss* necks. One special pattern is provided by a $(1+N_s)$-pattern with N_s in-buds and *ls* necks which contains no *ss* neck. All other pattern involve at least one *ss* neck which then determines the stability of these patterns, see the examples for $N_s = 2$, 3 and 4 in Figs. 16 and 17. The stability regimes for these different patterns again depend on the neck closure conditions for the necks which define two boundary lines within the morphology diagram, corresponding to the limit shapes L^{ls}_{1+Ns} and L^{ss}_{1+Ns},

see red and curved blue lines in Fig. 23. A third boundary line is provided by the line of touching spheres, arising from the physical constraint that the membrane of the multispherical shape should not intersect itself.

8.2.1. Limit shapes from closure of membrane necks

For negative spontaneous curvature, the dependence of the volume v on the small-sphere radius r_s is described by Eq. (77) and displayed in Fig. 21. As in the case of positive spontaneous curvature, we also parametrize the neck closure conditions in terms of the small-sphere radius r_s. The closure condition for *ss* necks then leads to the spontaneous curvature

$$\overline{m} = \overline{m}_{\rm ss}(r_s) = \frac{1}{2}(\overline{M}_s + \overline{M}_s) = -\frac{1}{r_s} \tag{96}$$

whereas the closure condition for *ls* necks becomes

$$\overline{m} = \overline{m}_{\rm ls}(r_s) = \frac{1}{2}\left(\frac{1}{\sqrt{1-N_s r_s^2}} - \frac{1}{r_s}\right), \tag{97}$$

where the first term represents the inverse large-sphere radius $1/r_l$. The corresponding boundary lines of limit shapes can then be obtained by parametric plots in the morphology diagram, combining the r_s-dependence of the volume v in Eq. (77) with the neck closure conditions in Eqs. (97) or (96) for *ls* and *ss* necks. When this method is used for (1 + 2)- and (1 + 15)-multispheres, one obtains the boundary lines $L^{\rm ls}_{1+{\rm Ns}}$ and $L^{\rm ss}_{1+{\rm Ns}}$ in Fig. 23.

8.2.2. Mechanical membrane tension

The mechanical membrane tension Σ is again given by $\Sigma = 2\kappa m(M_l + M_s - m)$ as in Eq. (85) and vanishes for $m = M_l + M_s$. Thus the mechanical tension vanishes for

$$\overline{m} = 2\overline{m}_{\rm ls}(r_s) = \frac{\sqrt{N_l}}{\sqrt{1-N_s r_s^2}} - \frac{1}{r_s} \tag{98}$$

which satisfies $\overline{m}_{\rm ss}(r_s) < 2\overline{m}_{\rm ls}(r_s) < \overline{m}_{\rm ls}(r_s)$ for negative spontaneous curvature. Therefore, the line of $(1 + N_s)$-multispheres with vanishing tension, corresponding to the purple lines in Fig. 23a and b, is now located between the two lines of limit shapes $L^{\rm ss}_{1+{\rm Ns}}$ and $L^{\rm ls}_{1+{\rm Ns}}$.

When we keep the volume v fixed but change the negative spontaneous curvature $\overline{m}$ to large negative values the geometry of the $(N_l + N_s)$-multisphere remains unchanged which implies that $M_l + M_s$ remains constant as well. Therefore, the mechanical tension behaves as

$$\Sigma \approx -2\kappa m^2 \quad \text{for large negative } m, \tag{99}$$

which is the same asymptotic behavior as for large positive m.

Using the neck closure conditions $M_l + M_s = 2m$ for *ls* necks, we obtain the positive mechanical tension

$$\Sigma = 2\kappa m^2 > 0 \quad \text{for the limit shapes } L^{\rm ls}_{1+{\rm Ns}} \tag{100}$$

which are located along the red boundary lines in Fig. 23. On the other hand, using the neck closure condition $M_s = m$ for *ss* necks, the mechanical tension now attains the negative values

$$\Sigma = 2\kappa m M_l < 0 \quad \text{for the limit shapes } L^{\rm ss}_{1+{\rm Ns}} \tag{101}$$

which are located along the curved blue lines in Fig. 23. Thus, the membranes of the limit shapes $L^{\rm ss}_{1+{\rm Ns}}$ now experience a negative tension Σ, in contrast to the positive mechanical tension for the limit shapes $L^{\rm ls}_{1+{\rm Ns}}$.

8.3. Instabilities of multispherical shapes via neck opening

It is instructive to consider an $(N_l + N_s)$-multisphere pattern, which is characterized by values of $\overline{m}$ and v that belong to the corresponding stability regime, and to explore the different trajectories in the morphology diagram by which one may open up the closed membrane necks. When we increase the volume of such a multisphere vesicle by osmotic inflation, we cross the boundary line L_{Nl+Ns} at which the least stable neck starts to open up. For (1 + 2)-multispheres and positive spontaneous curvature, for example, this neck opening occurs along the two boundary lines $L^{\rm ss}_{1+2}$ and $L^{\rm ls}_{1+2}$ in Fig. 22a. If the (1 + 2)-multiphere

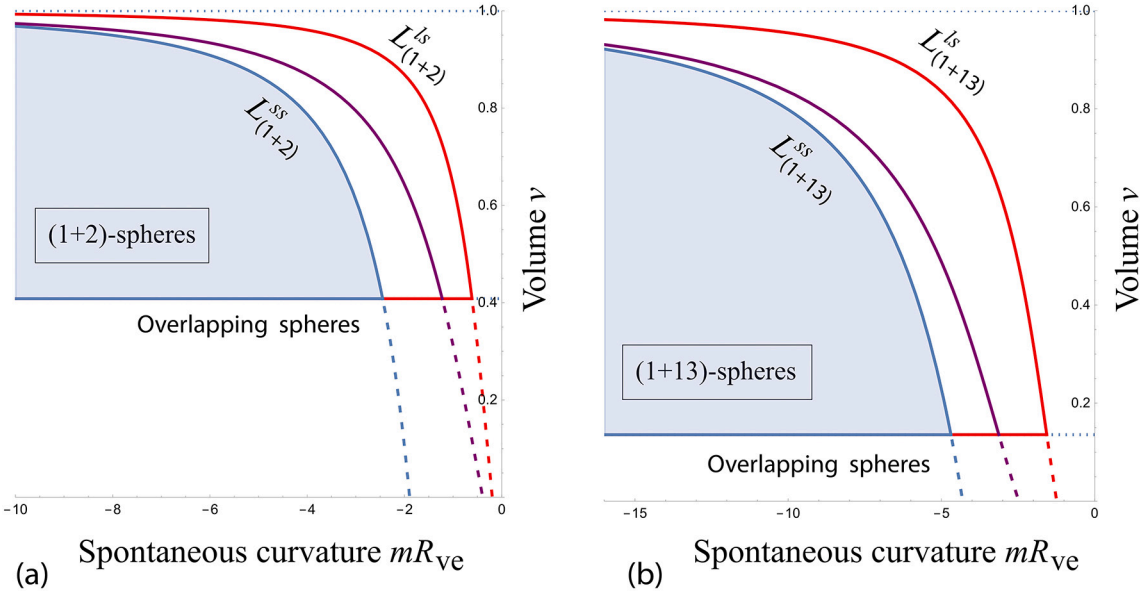

Fig. 23. Stability regimes of (1 + 2)- and (1 + 13)-multisphere patterns for negative spontaneous curvature. In both cases, the stability regime involves two boundary lines of limit shapes, denoted by $L^{\rm ls}_{1+{\rm Ns}}$ (red lines) and $L^{\rm ss}_{1+{\rm Ns}}$ (curved blue lines): (a) The two (1 + 2)-patterns in Fig. 16 are both stable within the blue-shaded region. In addition, the pattern with two in-buds and two *ls* necks is also stabe in the intermediate region between the boundary lines for $L^{\rm ls}_{1+{\rm Ns}}$ and $L^{\rm ss}_{1+{\rm Ns}}$. Along the purple lines, the mechanical tension Σ of the multispheres vanishes. One notable difference to the case with positive spontaneous curvature is that all $(1 + N_s)$-patterns with at least one *ss* neck experience a negative mechanical tension that acts to compress the vesicle membrane. (For interpretation of the references to color in this figure legend, the reader is referred to the web version of this article.)

forms the (1 + 2)-pattern $\mathcal{P}_1$ with one *ss* and one *ls* neck as in Figs. 13a and 1b, the *ss* neck opens up along the boundary line L^{ss}_{1+2} in Fig. 22a. If the (1 + 2)-multisphere forms the (1 + 2)-pattern $\mathcal{P}_1$ with two *ls* necks and two out-buds, the *ls* necks open up along the boundary line L^{ls}_{1+2}. Analogous behavior applies to (1 + 2)-multispheres and negative spontaneous curvature, for which the two boundary lines are displayed in Fig. 23a.

When we start from an $(N_l + N_s)$-multisphere pattern within its stability regime and decrease the volume by osmotic deflation, we reach two different boundary lines for positive and negative spontaneous curvature. For positive spontaneous curvature, we cross the boundary line L_{N^*} of $N_* = N_l + N_s$ equally sized spheres, at which all ** necks start to open up. For negative spontaneous curvature, we will reach the boundary line at which the small spheres start to touch each other and attain their most closely packed state. A third direction by which we can leave the stability regime of a multisphere is by decreasing the spontaneous curvature m for positive m and by increasing it for negative m. In both cases, we will again cross the boundary line L_{Nl+Ns}, at which the least stable necks of the multisphere pattern start to open up.

Finally, yet another pathway for neck opening of a multisphere is provided by external forces that are locally applied to the multisphere. So far, the corresponding elastic response of the multisphere has not been determined in a systematic manner. However, in view of the curvature-induced constriction forces as given by Eqs. (38) and (39), it seems likely that the necks open up when the locally applied forces exceed certain threshold values that are proportional to the constriction forces.

9. Summary and outlook

In this review, multispherical shapes of vesicles have been addressed theoretically for vesicle membranes with positive and negative values of the spontaneous curvature. For positive spontaneous curvature, $m > 0$, the membranes can form $(N_l + N_s)$-multispheres consisting of N_l large spheres and N_s small spheres, see the optical images in Fig. 1 as well as the cartoons in Figs. 13 and 14. One important consequence of curvature elasticity is that each $(N_l + N_s)$-multisphere involves only two different radii, with all large and all small spheres having the same radius R_l and R_s, respectively. For each value of N_l and N_s, the multispheres exhibit distinct patterns which differ in the way in which the spheres are mutually connected. As far as the stability of these patterns is concerned, we have to distinguish patterns with at least one *ss* neck between two small spheres from those with no *ss* neck but at least one *ls* neck between a large and a small sphere. The two types of patterns differ in their stability regimes as illustrated in Fig. 22 for (1 + 2)- and (1 + 15)-patterns.

For positive spontaneous curvature, multispheres with $N_* = N_l + N_s$ equally sized spheres are also possible, see optical images in Fig. 8 and cartoons in Fig. 15. These shapes represent limit shapes, denoted by L_{N^*}, which are constant-mean-curvature surfaces and have the remarkable property that they provide a boundary line for all $(N_l + N_s)$-multispheres with $N_l + N_s = N_*$. For $N_l + N_s = 3$, for example, the multispheres form two (1 + 2)-patterns and two (2 + 1)-patterns, see Fig. 13. All four patterns approach the limit shapes L_{3^*} when we reduce the volume v towards its lowest possible value $v_* = 1/\sqrt{3}$. This degeneracy of the L_{N^*}-multispheres increases strongly with the sphere number N_*.

For negative spontaneous curvature, $m < 0$, the membranes can form $(1 + N_s)$-multispheres, see the optical images in Fig. 2 as well as the cartoons in Figs. 16 and 17, consisting of one large sphere that encloses N_s small spheres. For each value of N_s, the multispheres exhibit distinct patterns in which the spheres are connected in different ways. For $m < 0$, only one pattern, corresponding to N_s in-buds, has no *ss* neck whereas all other patterns involve at least one *ss* neck. The two types of patterns differ again in their stability regimes as illustrated in Fig. 23 for (1 + 2)- and (1 + 13)-patterns. For $N_s \geq 3$, the small spheres can form junctions, at which a central small sphere is connected to three or more neighboring small spheres. Now, the physical requirement that the spheres should not overlap or, equivalently, that the membrane should not self-intersect leads to the smallest possible value $v = v_{cp}$ corresponding to close packing the small spheres within the large sphere. Some examples for the numerical value of v_{cp} are provided in Table 1

In order to keep the length of this paper within reasonable limits, several aspects of multispheres have not been addressed here. These aspects include (i) the elastic energy landscape of the multispheres, (ii) the stability of individual spheres with respect to sphere-prolate bifurcations, and (iii) the curvature-induced fission of membrane necks for sufficiently large absolute values of the spontaneous curvature. All three aspects have been theoretically examined in Ref. [17], at least to some extent. The elastic energy landscape is quite 'rugged' and exhibits many metastable states as described in Ref. [75] for $(1 + N_s)$-multispheres with negative spontaneous curvature. The sphere-prolate bifurcation leads to an upper boundary for the spontaneous curvature, which has been used to estimate the spontaneous curvature of the multispheres in Fig. 1 [13]. The fission of a single membrane neck has been experimentally demonstrated for giant two-sphere vesicles in Ref. [40] where the controlled division of these vesicles into two daughter vesicles has been observed.

Many interesting aspects of multispherical shapes remain to be explored. First, the constriction forces acting at membrane necks could be used experimentally to drive the controlled division of multispheres with more than one neck. The constriction force f_{ls} at an *ls* neck exceeds the constriction force f_{ss} at an *ss* neck, as described by Eq. (40) for positive spontaneous curvature and by Eq. (41) for negative spontaneous curvature. Therefore, for given values of spontaneous curvature $\overline{m}$ and volume v, the *ls* necks are more likely to be cleaved compared to the *ss* necks. Likewise, when the necks are opened by locally applied external forces, these forces should exceed certain threshold values that are proportional to the curvature-dependent constriction forces f_{ls} and f_{ss}.

Second, when combined with changes in the osmotic conditions, the fine-tuning of the spontaneous curvature by His-tagged GFPs [40] could be used to create multispherical shapes with more than one neck in a controlled manner. The creation of stable multispheres could be further improved by experimental methods that induce membrane fusion. One could start from spherical vesicles which are exposed to curvature-generating molecules such as His-tagged GFP. When two such vesicles are fused, a two-sphere vesicle is formed. This two-sphere vesicle is stable if the volume and the spontaneous curvature are located within the corresponding stability regime. When we fuse a third spherical vesicle with the two-sphere vesicle, we should obtain a stable three-sphere vesicle provided we match the radius of the third sphere with one sphere radius of the two-sphere shape. Otherwise, we expect to see interesting relaxation processes that may involve the opening of membrane necks. Using membrane fusion, we should also be able to create multispherical shapes that have a more complex higher-genus topology with closed cycles of spheres. Finally, it would be rather interesting to consider multispherical shapes using membranes with two types of coexisting lipid phase domains. Two-sphere vesicles formed by membranes with two different lipid domains have been studied theoretically [68,93] and, to some extent, experimentally [94–96]. The theory also predicts that membranes with coexisting lipid phase domains can form more complex $(N_l + N_s)$-multispheres that involve more than two different sphere radii [17]. Such more complex multispherical shapes remain to be studied in a systematic manner, both theoretically and experimentally[2].

[2] The adsorption of Ca^{2+} ions onto negatively charged membranes generates membrane tubules that point away from the solution with the higher Ca^{2+} concentration [97], in agrement with the concentration-dependent reduction of the area per lipid discussed in Section 2.2.

Declaration of Competing Interest

The author declares no conflict of interest.

Acknowledgments

I thank Tripta Bhatia, now at the IISER Mohali, for sharing the unpublished image in Fig. 9c with me, Rumiana Dimova for drawing my attention to Ref. [97], and all my collaborators for enjoyable and fruitful interactions. This research was conducted within the Max Planck School Matter to Life supported by the German Federal Ministry of Education and Research (BMBF) in collaboration with the Max Planck Society and the Max Planck Institute of Colloids and Interfaces.

References

[1] Gorter E, Grendel F. On bimolecular layers of lipoids on the chromocytes of the blood. J Exp Med 1925;41:439–43.
[2] Robertson JD. The ultrastructure of cell membranes and their derivatives. Biochem Soc Symp 1959;16:3–43.
[3] Robertson JD. The molecular structure and contact relationships of cell membranes. Prog Biophys Bio Ch 1960;10:343–418.
[4] Kornberg RD, McConnell HM. Lateral diffusion of phospholipids in a vesicle membrane. Proc Nat Acad Sci USA 1971;68:2564–8.
[5] Sackmann E, Träuble H. Studies of the crystalline-liquid crystalline phase transition of lipid model membranes ii: analysis of electron spin resonance spectra of steroid labels incorporated into Lipid Membranes. JACS 1972;94:4492–8.
[6] Canham PB. The minimum energy of bending as a possible explanation of the biconcave shape of the human red blood cell. J Theor Biol 1970;26:61–81.
[7] Helfrich W. Elastic properties of lipid bilayers: theory and possible experiments. Z Naturfor 1973;28c:693–703.
[8] Evans EA. Bending resistance and chemically induced moments in membrane bilayers. Biophys J 1974;14:923–31.
[9] Singer SJ, Nicolson GL. The fluid mosaic model of the structure of cell membranes. Science 1972;175:720–31.
[10] Bassereau P, Sens P. Physics of biological membranes. Springer Nature; 2018. editors.
[11] Dimova R, Marques C. The giant vesicle book. Taylor & Francis; 2020. editors.
[12] Lipowsky R, Dimova R. Introduction to remodeling of biomembranes. Soft Matt 2021;17:214–21.
[13] Bhatia T, Christ S, Steinkühler J, Dimova R, Lipowsky R. Simple sugars shape giant vesicles into multispheres with many membrane necks. Soft Matt 2020;16:1246–58.
[14] van Meer G, Voelker DR, Feigenson GW. Membrane lipids: where they are and how they behave. Nat Rev: Mol Cell Biol 2008;9:112–24.
[15] Fadeel B, Xue D. The ins and outs of phospholipid asymmetry in the plasma membrane: roles in health and disease. Crit Rev Biochem Mol Biol 2009;44:264–77.
[16] Lipowsky R. Understanding and controlling the morphological complexity of biomembranes. Multiresponsive behavior of biomembranes and giant vesicles, volume 30 of advances in biomembranes and lipid self-assembly. Academic press; 2019. p. 105–55. chapter 3.
[17] Lipowsky R. Understanding giant vesicles: a theoretical perspective. In: Dimova R, Marques C, editors. The giant vesicle book. Taylor & Francis; 2020. p. 73–168. chapter 5.
[18] Lipowsky R. Coupling of bending and stretching deformations in vesicle membranes. Adv Colloid Interface Sci 2014;208:14–24.
[19] Bassereau P, Jin R, Baumgart T, Deserno M, Dimova R, Frolov VA, Baskirov PV, Grubmüller H, Jahn R, Risselada HJ, Johannes L, Kozlov MM, Lipowsky R, Pucadyil TJ, Zeno WF, Stachowiak JC, Stamou D, Breuer A, Lauritsen L, Simon C, Sykes C, Voth GA, Weikl TR. The 2018 biomembrane curvature and remodeling roadmap. J Phys D: Appl Phys 2018;51:343001.
[20] Różycki B, Lipowsky R. Spontaneous curvature of bilayer membranes from molecular simulations: asymmetric lipid densities and asymmetric adsorption. J Chem Phys 2015;142:054101.
[21] Ghosh R, Satarifard V, Grafmüller A, Lipowsky R. Spherical nanovesicles transform into a multitude of nonspherical shapes. Nano Lett 2019;19:7703–11.
[22] Sreekumari A, Lipowsky R. Lipids with bulky head groups generate large membrane curvatures by small compositional asymmetries. J Chem Phys 2018;149:084901.
[23] Dasgupta R, Miettinen MS, Fricke N, Lipowsky R, Dimova R. The glycolipid GM1 reshapes asymmetric biomembranes and giant vesicles by curvature generation. Proc Nat Acad Sci USA 2018;115:5756–61.
[24] Miettinen M, Lipowsky R. Bilayer membranes with frequent flip flops have tensionless leaflets. Nano Lett 2019;19:5011–6.
[25] Lipowsky R, Döbereiner HG. Vesicles in contact with nanoparticles and colloids. Europhys Lett 1998;43:219–25.
[26] Różycki B, Lipowsky R. Membrane curvature generated by asymmetric depletion layers of ions, small molecules, and nanoparticles. J Chem Phys 2016;145:074117.
[27] Lipowsky R. Spontaneous tubulation of membranes and vesicles reveals membrane tension generated by spontaneous curvature. Faraday Disc 2013;161:305–31.
[28] Ghosh R, Satarifard V, Grafmüller A, Lipowsky R. Budding and fission of nanovesicles induced by membrane adsorption of small solutes. ACS Nano 2021;15:7237–48.
[29] Simunovic M, Lee KYC, Bassereau P. Celebrating soft matter's 10th anniversary: screening of the calcium-induced spontaneous curvature of lipid membranes. Soft Matt 2015;11:5030–6.
[30] Graber ZT, Shi Z, Baumgart T. Cations induce shape remodeling of negatively charged phospholipid membranes. PCCP 2017;19:15285–95.
[31] Melcrov A, Pokorna S, Pullanchery S, Kohagen M, Jurkiewicz P, Hof M, Jungwirth P, Cremer PS, Cwiklik L. The complex nature of calcium cation interactions with phospholipid bilayers. Sci Rep 2016;6:38035.
[32] Kučerka N, Ermakova E, Dushanov nad E, Kholmurodov KT, Kurakin S, Želinská K, Uhriková D. Cation-zwitterionic lipid interactions are affected by the lateral area per lipid. Langmuir 2021;37:278–88.
[33] Balantič K, Weiss U, Allmaier G, Kramar P. Calcium ion effect on phospholipid bilayers as cell membrane analogues. Bioelectrochemistry 2022;143:107988.
[34] Agudo-Canalejo J, Lipowsky R. Critical particle sizes for the engulfment of nanoparticles by membranes and vesicles with bilayer asymmetry. ACS Nano 2015;9:3704–20.
[35] Lipowsky R. Bending of membranes by anchored polymers. Europhys Lett 1995;30:197–202.
[36] Lipowsky R, Döbereiner HG, Hiergeist C, Indrani V. Membrane curvature induced by polymers and colloids. Physica A 1998;249:536–43.
[37] Nikolov V, Lipowsky R, Dimova R. Behavior of giant vesicles with anchored DNA molecules. Biophys J 2007;92:4356–68.
[38] Chen Z, Atafi E, Baumgart T. Membrane shape instability induced by protein crowding. Biophys J 2016;111:1823–6.
[39] Snead WT, Hayden CC, Gadok AK, Zhao C, Lafer EM, Rangamani P, Stachowiak JC. Membrane fission by protein crowding. Proc Nat Acad Sci USA 2017;114:E3258–67.
[40] Steinkühler J, Knorr RL, Zhao Z, Bhatia T, Bartelt S, Wegner S, Dimova R, Lipowsky R. Controlled division of cell-sized vesicles by low densities of membrane-bound proteins. Nat Commun 2020;11:905.
[41] Peter BJ, Kent HM, Mills IG, Vallis Y, Butler PJG, Evans PR, McMahon HT. BAR domains as sensors of membrane curvature: the amphiphysin bar structure. Science 2004;303:495–9.
[42] McMahon HT, Gallop JL. Membrane curvature and mechanisms of dynamic cell membrane remodelling. Nature 2005;438:590–6.
[43] Sorre B, Callan-Jones A, Manzi J, Goud B, Prost J, Bassereau P, Roux A. Nature of curvature coupling of amphiphysin with membranes depends on its bound density. PNAS 2012;109(1):173–8.
[44] Loerke D, Mettlen M, Yarar D, Jaqaman K, Jaqaman H, Danuser G, Schmid SL. Cargo and dynamin regulate clathrin-coated pit maturation. PLOS Biol 2009;7(3):e1000057.
[45] Cureton DK, Harbison CE, Parrish CR, Kirchhausen T. Limited transferrin receptor clustering allows rapid diffusion of canine parvovirus into clathrin endocytic structures. J Virol 2012;86(9):5330–40.
[46] Lizarrondo J, Klebl DP, Niebling S, Abella M, Schroer MA, Mertens HDT, Veith K, Thuenauer R, Svergun DI, Skruzny M, Sobott F, Muench SP, Garcia-Alai MM. Structure of the endocytic adaptor complex reveals the bais for efficient membrane anchoring during clathrin-mediated endocytosis. Nat Commun 2021;12:2889.
[47] Shin J, Nile A, Oh J-W. Role of adaptin protein complexes in intracellular trafficking and their impact on diseases. Bioengineered 2021;12(1):8259–78.
[48] Vigers GPA, Crowther RA, Pearse BMF. Location of the 100 kDa-50 kDa accessory proteins in clathrin coats. EMBO J 1986;5(9):2079–85.
[49] Chithrani BD, Ghazani AA, Chan WCW. Determining the size and shape dependence of gold nanoparticle uptake into mammalian cells. Nano Lett 2006;6(4):662–8.
[50] Chithrani BD, Chan WCW. Elucidating the mechanism of cellular uptake and removal of protein-coated gold nanoparticles of different sizes and shapes. Nano Lett 2007;7(6):1542–50.
[51] Deuling HJ, Helfrich W. The curvature elasticity of fluid membranes: a catalogue of vesicle shapes. J Phys 1976;37:1335–45.
[52] Seifert U, Berndl K, Lipowsky R. Shape transformations of vesicles: phase diagram for spontaneous curvature and bilayer coupling model. Phys Rev A 1991;44:1182–202.
[53] Delaunay C. Sur la surface de révolution dont la courbure moyenne est constante. J Math Pures Appl Sér 1841;6:309–20.
[54] Kapouleas N. Complete constant mean curvature surfaces in euclidean three-space. Ann Math 1990;131:239–330.
[55] Korevaar NJ, Kusner R, Solomon B. The structure of complete embedded surfaces with constant mean curvature. J Diff Geomet 1989;30:465–503.
[56] Korevaar N, Kusner R. The global structure of constant mean curvature surfaces. Invent Math 1993;114:311–32.
[57] Grosse-Brauckmann K, Polthier K. Constant mean curvature surfaces derived from delaunay's and wente's examples. In: Hege HC, Polthier K, editors. Visualization and mathematics. Springer Verlag; 1997. p. 386.
[58] Grosse-Brauckmann K, Kusner RB, Sullivan JM. Triunduloids: embedded constant mean curvature surfaces with three ends and genus zero. J Fur Die Reine Und Angewandte Mathemat 2003;564:35–61.
[59] Ou-Yang Z-C, Helfrich W. Bending energy of vesicle membranes: general expressions for the first, s econd and third Variation of the shape energy and applications to spheres and cylinders. Phys Rev A 1989;39:5280–8.
[60] Mladenov IM, Hadzhilazova M, Opera J. Unduloids and their geometry. Arch Math 2007;43:417–29.

[61] Bessis M. Living blood cells and their ultrastructure. Berlin-Heidelberg-New York: Springer; 1973.
[62] Deuling HJ, Helfrich W. A theoretical explanation for the myelin shapes of red blood cells. Blood Cells 1977;3:713–20.
[63] Bar-Ziv R, Moses E. Instability and pearling states produced in tubular membranes by competition of curvature and tension. Phys Rev Lett 1994;73:1392–5.
[64] Goldstein RE, Nelson P, Powers T, Seifert U. Front propagation in the pearling instability of tubular vesicles. J Phys II France 1996;6:767–96.
[65] Tsafrir I, Guedeau-Boudeville MA, Kandel D, Stavans J. Coiling instability of multilamellar membrane tubes with anchored polymers. Phys Rev E 2001;63. 031603/1-11.
[66] Christ S, Litschel T, Schwille P, Lipowsky R. Active shape oscillations of giant vesicles with cyclic closure and opening of membrane necks. Soft Matt 2021;17: 319–30.
[67] Fourcade B, Miao L, Rao M, Wortis M, Zia RKP. Scaling analysis of narrow necks in curvature models of fluid lipid-bilayer vesicles. Phys Rev E 1994;49:5276–86.
[68] Jülicher F, Lipowsky R. Shape transformations of inhomogeneous vesicles with intramembrane domains. Phys Rev E 1996;53:2670–83.
[69] Lipowsky R. Remodeling of membrane compartments: some consequences of membrane fluidity. Biol Chem 2014;395:253–74.
[70] Terasaki M, Chen LB, Fujiwara K. Microtubules and the endoplasmic reticulum are highly interdependent structures. J Cell Biol 1986;103:1557–68.
[71] Lee C, Chen LB. Dynamic behavior of endoplasmic reticulum in living cells. Cell 1988;54:37–46.
[72] Dreier L, Rapoport TA. In vitro formation of the endoplasmic reticulum occurs independently of microtubules by a controlled fusion reaction. J Cell Biol 2000;148 (5):883–98.
[73] Nixon-Abell J, Obara CJ, Weigel AV, Li D, Legant WR, Shan Xu C, Pascolli HA, Harvey K, Hess HF, Betzig E, Blackstone C, Lippincott-Schwartz J. Increased spatiotemporal resolution reveals highly dynamic dense tubular matrices in th eperipheral ER. Science 2016;354. aaf3928.
[74] Powers RE, Wang S, Liu TY, Rapoport TA. Reconstruction of the tubular endoplasmic reticulum network with purified components. Nature 2017;543: 257–72.
[75] Yonggang Liu J, Agudo-Canalejo A, Grafmüller R, Dimova R, Lipowsky. Patterns of flexible nanotubes formed by liquid-ordered and liquid-disordered membranes. ACS Nano 2016;10:463–74.
[76] Gilbert EN, Pollak HO. Steiner minimal trees. SIAM J Appl Math 1968;16:1–29.
[77] Hildebrandt S, Tromba A. Mathematics and optimal form. American Scientific Library; 1985.
[78] MacGregor Smith J, Weiss R, Patel M. An O(N^2) heuristic for steiner minimal trees in E^3. Networks 1995;25:273–89.
[79] Prömel HJ, Steger A. The Steiner Tree Problem. Vieweg - Springer; 2002.
[80] Brazil M, Graham RL, Thomas DA, Zachariasen M. On the history of the euclidean steiner tree problem. Arch Hist Exact Sci 2014;68:327–54.
[81] Courant R, Robbins H. What is mathematics? New York: Oxford University Press; 1941.
[82] Dutta P, Khastgir SP, Roy A. Steiner trees and spanning trees in six-pin soap films. Am J Phys 2010;78(2):215–21.
[83] Garey MR, Graham RL, Johnson DS. The complexity of computing steiner minimal trees. SIAM J Appl Math 1977;32(4):853–9.
[84] Zachariasen M. Local search for the steiner tree problem in the euclidean plane. Eur J Oper Res 1999;119:282–300.
[85] Bridges R. Minimal steiner trees for three dimensional networks. Math Gaz 1994;78 (482):157–62.
[86] Kepler J. The six-cornered snowflake. Paul Dry Books; 2010.
[87] Hales TC, Ferguson SP. A formulation of the kepler conjecture. Discrete Comput Geom 2006;36:21–69.
[88] Hales T, Adams M, Bauer G, Dang TD, Harrison J, Hoang LT, Kalszyk C, Magron V, McLaughlin S, Nguyen TT, Nguyen QT, Nipkow T, Obua S, Pleso J, Rute J, Solevyev A, An Ta TH, Tran NT, Trieu TD, Urban J, Vu K, Zumkeller R. A formal proof of the kepler conjecture. Forum Math 2017;5:e2. Pi.
[89] Lagarias JC. The Kepler Conjecture and Its Proof. In: Lagarias JC, editor. The kepler conjecture: the hales-ferguson proof. Springer; 2011. p. 1–26.
[90] Scott GD, Kilgour DM. The density of random close packing of spheres. J Phys D: Appl Phys 1969;2:863–6.
[91] Jaeger HM, Nagel SR. Physics of the granular state. Science 1992;255:1523–31.
[92] Chaikin P. Random thoughts. Phys Today 2007;9:8–9.
[93] Lipowsky R. Budding of membranes induced by intramembrane domains. J Phys II France 1992;2:1825–40.
[94] Baumgart T, Hess ST, Webb WW. Imaging coexisting fluid domains in biomembrane models coupling curvature and line tension. Nature 2003;425: 821–4.
[95] Riske KA, Bezlyepkina N, Lipowsky R, Dimova R. Electrofusion of model lipid membranes viewed with high temporal resolution. Biophys Rev Lett 2006;1: 387–400.
[96] Dreher Y, Jahnke K, Bobkova E, Spatz JP, Göpfrich K. Division and regrowth of phase-separated giant unilamellar vesicles. Angew Chemie Int 2021;60:10661–9.
[97] Doosti BA, Pezeshkian W, Bruhn DS, Ipsen JH, Khandelia H, Jeffries GDM, Lobovkina T. Membrane tubulation in lipid vesicles triggered by the local application of calcium ions. Langmuir 2017;33:11010–7.